DEVELOPMENT OF A ROBOTIC BIOPSY SYSTEM COMPATIBLE WITH LABEL-FREE DIGITAL PATHOLOGY AND METHODS FOR NEEDLE-TISSUE CLASSIFICATION

BY

FANXIN WANG

DISSERTATION

Submitted in partial fulfillment of the requirements
for the degree of Doctor of Philosophy in Mechanical Engineering
in the Graduate College of the
University of Illinois Urbana-Champaign, 2023

Urbana, Illinois

Doctoral Committee:

      Professor Placid Mathew Ferreira, Chair
      Professor Thenkurussi Kesavadas, Director of Research
      Professor Naira Hovakimyan
      Professor Rohit Bhargava

ABSTRACT

The diagnosis of disease faces fundamental limitations due to the uncertainty surrounding the incremental benefits of tissue sampling and biopsy. In response to this critical challenge, a robotic biopsy system with compatibility with label-free digital pathology and methods for tissue classification was developed in this dissertation. This new system incorporates a steerable needle insertion system and is designed to compatible with digital pathology, granting access to tissues' chemical and molecular composition. The tissue classification method holds promise in enhancing the precision and depth of information obtainable through biopsy procedures.

In this research we have designed and developed a 5-degree-of-freedom (DOF) robotic biopsy system, integrated with a 3-DOF insertion module, which has been tested in various conditions. Helical motion functionality with detailed workspace analysis has been conducted to optimize the system reach. Safety control algorithms, including a hybrid force/position robotic platform control and semi-autonomous needle insertion control, have been developed to ensure the precision required for needle insertion procedures. Experiments have been carried out on both synthetic and real porcine tissues to validate the system performance.

To address a significant challenge in current biopsy procedures, specifically the difficulty surgeons face in accurately placing the needle tip, a novel classification method rooted in machine learning has been developed. Data has been collected from five different types of porcine tissues, and a transformer-based classification model has been trained after thorough data pre-processing. The results have been compared with other state-of-the-art methods, revealing that this new transformer-based classification method is more precise and effective in tissue type detection. This innovation holds potential as a valuable tool for surgeons, by enhancing surgeon awareness and precision. This advancement contributes to the overall success of the biopsy process by providing a new in-situ process that does not exist today.

The combination of the robotic biopsy system and the learning-based classification methodology holds the potential to improve the field of needle biopsy. By providing accurate and precise needle placement, access to tissue composition, and real-time environment recognition, the groundwork is laid for the creation of an accurate computer-aided digital needle biopsy system.

ACKNOWLEDGMENTS

I am deeply grateful for the invaluable advice, assistance, and guidance that have been instrumental in the successful completion of this thesis. First, I wish to express my profound gratitude to Professor Thenkurussi Kesavadas for his unwavering support throughout my Ph.D. journey and the associated research. His patience, motivation, and vast reservoir of knowledge have been invaluable. His guidance was an essential pillar throughout the research and writing of this thesis.

In addition to my advisor, I extend my heartfelt gratitude to the rest members of my thesis committee: Professor Placid Ferreira, Professor Rohit Bhargava, and Professor Naira Hovakimyan. Their insightful comments and valuable feedback have been instrumental in guiding me to this point in my academic journey.

I would like to express my sincere appreciation to my fellow lab mates and the dedicated staff at the Health Care Engineering Systems Center. I extend my gratitude to Xiao, Sudipta, Yao, Naveen, Srikar, Kuocheng, Anusha, Harris, Tony, and Michelle for the wonderful moments we have shared.

Last but certainly not least, I wish to express my deepest gratitude to my family, for their unwavering spiritual support throughout my thesis journey and in my life.

To my family for their love and support.

TABLE OF CONTENTS

LIST OF FIGURES

CHAPTER 1

INTRODUCTION

1.1 Background and Motivation

The diagnostic approach for understanding the underlying causes of cancers, along with numerous other diseases, encounters formidable limitations. Central to these limitations is the uncertainty surrounding the incremental benefits of tissue sampling and biopsy procedures. Several factors contribute to this uncertainty. In response to these limitations, the medical field has explored advanced techniques to enhance diagnostic accuracy during different biopsy procedures [1]. Beyond basic imaging systems of CT, MRI or ultrasound, there are electroanatomic mapping, cardiac magnetic resonance imaging (CMR), and positron emission tomography to enhance accuracy. These technologies have been utilized to guide the biopsy process more effectively, enabling the sampling of precisely affected myocardial regions. For instance, electroanatomic mapping provides real-time guidance by creating detailed electrical maps of the heart, aiding in pinpointing the areas of interest. CMR [1] offers excellent visualization capabilities, allowing for the identification of myocardial abnormalities. While these advanced techniques hold promise in improving the diagnostic accuracy of different biopsies, it's important to note that they are not yet widely accessible or routinely performed. Factors such as equipment availability, expertise required for interpretation, and cost constraints may limit their use in clinical practice.

In actual surgical situations, surgeons still rely on their intuition to measure the variances in tissue properties while performing manual needle interventions. They employ this

perception to identify anatomical structures and events, including puncture occurrences and the differentiation between soft and hard tissues. This is made possible through the haptic feedback derived from the interaction between the needle and the tissue. In breast cancer diagnosis research [2], it was asserted that the mean shear stiffness of breast carcinoma is approximately 418% higher than the mean value of the surrounding breast tissues. Researchers have utilized the significance of interaction force change between the needle and the tissue to develop classifiers for distinguishing fundamental tissue properties. Statistical models are used for the classification of liver needle insertion based on force patterns [3], Young's modulus is identified based on the energy stored in the needle-tissue system [4], a recurrent neural network (RNN) based Long-Short Term Memory (LSTM) model was trained to estimate the various synthetic tissue classes [5]. This research validated the concept that the integration of a force parameter with position data can enhance the comprehension of interactions in a wide range of interventional procedures and diagnostic processes.

Recent developments in robotic biopsy are also making significant impacts on various usage in different disease diagnoses. It excels in performing precise and accurate needle insertions with the assistance of imaging systems [6]. Robotic biopsy procedures have been employed in diverse anatomical sites, such as bone [7], lung [8], breast [9], brain or brainstem [10], prostate [11], and liver [12]. Robotic biopsy demonstrates its advantages in maintaining a straight-line trajectory, with guidance primarily relying on standard radiological images. These types of interventions exemplify how robotics enhances precision by seamlessly integrating imaging with precise procedural guidance [6]. However, there have been fewer reported cases of robotic assistance in the field of endomyocardial biopsy. In 2018, researchers [13] pioneered the application of robotic assistance to address the patchy and unpredictable nature of infiltrate locations in traditional endomyocardial biopsy. Yet, the potential benefits provided by robotic

applications within hospital settings, such as improved accuracy, precision, consistent execution of small tasks, enhanced ergonomics, and resistance to fatigue, have not been fully realized. There appears to be a gap between advanced robotic technology and the practical clinical needs [6].

The diagnostic process still requires that the biopsy be taken to pathology, sectioned and stained before a pathologist can visually examine histologic images under a microscope and diagnose. The execution of this procedure demands substantial resources, specialized expertise, and a significant time investment to generate a comprehensive diagnosis report. Furthermore, a majority of the biopsy specimens may be normal and not diagnostic of any specific process – in these cases, it would be optimal to not obtain a sample as otherwise it injures normal tissue [14]. The past two decades have seen the development of many in-vitro imaging techniques [15] that are based on optical spectroscopy. By utilizing the refractive index, absorption, scattering, or native fluorescence signatures of tissue as contrast, molecular images can be obtained. One extensively employed technique in medical imaging is fluorescence imaging [16]. Raman spectroscopic analysis and infrared spectroscopic analysis represent two key domains closely associated with fluorescence imaging [17]. in In-vivo stimulated Raman scattering microscopy (SRSM) [17] circumvents the above limitations by probing the vibrations of the molecular constituents in tissues, similar to infrared spectroscopy. However, SRSM is an expensive technique, and suffers from the inherently smaller signal to noise of Raman spectroscopy over infrared. In contrast to infrared spectroscopy, Raman spectroscopy is characterized by higher costs and inherent signal limitations. The progress marked by the introduction of fast Fourier transform (FT), the advancements in FT-IR spectrometers, and the integration of cutting-edge technologies in IR spectroscopy has significantly elevated computational and data handling capabilities in label-free digital pathology, ensuring heightened accuracy and efficiency.

In response to the challenges posed by the absence of haptic feedback, limited adaptability in robotic systems, and the time-intensive nature of traditional pathology procedures, our primary focus is devising solutions to offer a rapid and accurate platform for robotic biopsies. Furthermore, we seek to facilitate the integration of fiber-optic tools for digital pathology. To realize these objectives, we have designed a robotic system equipped with a steerable needle insertion module that is fully compatible with in-situ, fiber-optic-based vibrational spectroscopy. We have also established a standardized experimental setup using the robotic system to collect data, which is subsequently employed to train a transformer-based tissue classification model. The primary aim of this model is to empower surgeons with the ability to recognize the tissue environment during needle biopsies. Our research aims to develop technology that leverages the potential digital pathology, guided by robotics operated by surgeons under the aid in haptic environmental recognition, to target specific regions of interest in an accurate and fast way.

1.2 Dissertation Overview

In the remainder of this thesis, we present the development of the fiber-optic compatible robotic biopsy system and the classification of transition in different tissues. The organization of the dissertation is as the following:

- Chapter 2 presents the literature review for biopsy in medical diagnosis, detailed needle biopsy procedures and limitations, recent work in robotic biopsy platforms and digital pathology, summarized with our research goal.
- Chapter 3 presents the design and development of the fiber-optic compatible robotic biopsy system, shows its compatibility with label-free digital pathology. Then, we conduct the mathematical modeling of robot dynamics and demonstrate future work in the robotic platform.

- Chapter 4 presents the semi-autonomous safety control architecture. Hybrid force/position control and semi-autonomous position control are introduced. Performance and safety evaluations are then carried out.

- Chapter 5 presents transformer-based tissue classification for biopsy. Mechanics in needle-tissue interaction is modeled first. Then, the transformer model for classification and prediction is introduced. Detailed experiment setup and data collection are demonstrated. The result and evaluation of classification are carried out under certain evaluation metrics after model training. Discussion includes a model expansion into force prediction and future AI integration on robotic biopsy.

- Chapter 6 presents the concluding remarks. Also, chapter 6 suggests the possible future directions of research.

1.3 Dissertation Contribution

An accurate computer-aided needle biopsy system is founded for higher performance in the needle biopsy field. Our results can be summarized as follows:

<u>Design and development of the novel digital pathology compatible robotic biopsy system:</u>
- Design and development of a novel robotic biopsy system with high dexterity, modeling the workspace and dynamics to fully discover the capability of the biopsy system.

- Development of the novel fiber-optic compatibility with the robotic biopsy system, which leads to the next generation of digital pathology integrated with robotic precision.

- Development of a semi-autonomous safety control for the robotic system, ensuring the precision of robotic movement with safety concerns.

Development of a novel intelligent system for robotic biopsy assistance system:

- Modeling of the mechanics of needle-tissue interaction. Formalize a deep-learning integrated model to describe the transitions during needle-tissue interactions based on needle insertion force.

- With data collection on experiment setup with the robotic platform, the transformer model for classification is trained and evaluated. The proposed methodology outperforms the current state-of-art methodology in all evaluation metrics.

- Expand the classification model into force prediction. Establish a novel transformer model for force prediction to aid surgeons during the insertion process. Proposing the next generation of artificial intelligence in robotic biopsy assistance.

CHAPTER 2

LITERATURE REVIEW

2.1 Biopsy in Medical Diagnosis

The biopsy is a medical procedure in which a sample of tissue or cells is extracted from the body for subsequent laboratory testing. It has evolved into a fundamental component of contemporary medicine [18], and a majority of biopsies in modern healthcare are conducted percutaneously with the assistance of image-guided techniques. The biopsy can be performed on various target tissues in the body to diagnose or evaluate different medical conditions. The choice of target tissue depends on the specific clinical scenario and the suspected disease. Solid tumor and masses diagnosing would include biopsies for breast, prostate, liver, lung and kidney tissues [19]. Lymph node biopsies can determine the presence of infections, malignancies, or autoimmune disorders [20]. Bone marrow biopsies help diagnose blood disorders, leukemia, and certain bone conditions [21]. Skin biopsies are commonly performed to diagnose dermatological conditions, including skin cancer, rashes, and infections [22]. Brain biopsies are performed in some cases to diagnose brain tumors, infections, or neurological disorders [23].

Regarding the differences in tools and procedures of biopsy, biopsy can be categorized into needle biopsy, surgical biopsy, endoscopic biopsy, bone marrow biopsy or skin biopsy.

A needle biopsy encompasses several techniques, including fine-needle aspiration, core needle biopsy, and vacuum-assisted biopsy [24]. These methods are employed to collect tissue or cell samples for diagnostic purposes. Image-guided biopsy procedures are

particularly valuable when dealing with areas that cannot be palpated through the skin, such as those in the liver, lung, or prostate. By utilizing real-time imaging, surgeons can precisely guide the biopsy needle to the target area, ensuring accurate sample collection.
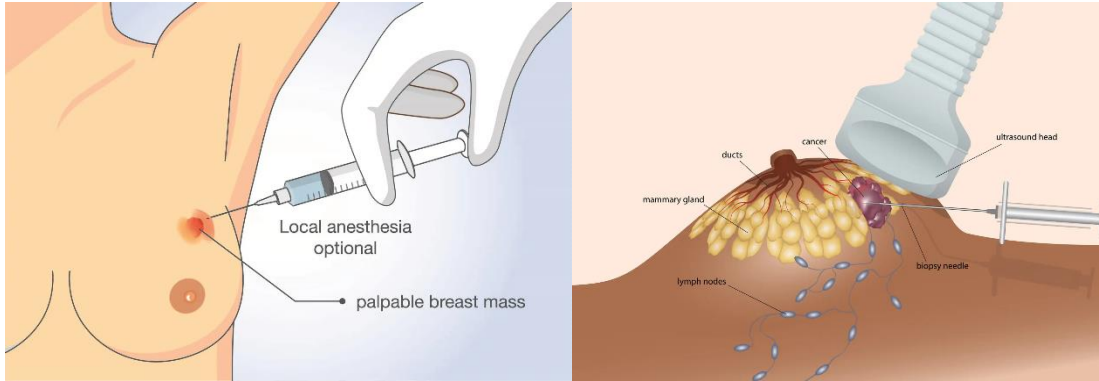
Figure 2.1: Fine needle aspiration biopsy(left) vs core needle biopsy with ultrasound(right)

Endoscopic biopsy is a procedure in that surgeons would use a thin, flexible tube (endoscope) with a light on the end to see structures inside your body. Special tools are passed through the tube to take a small sample of tissue to be analyzed.
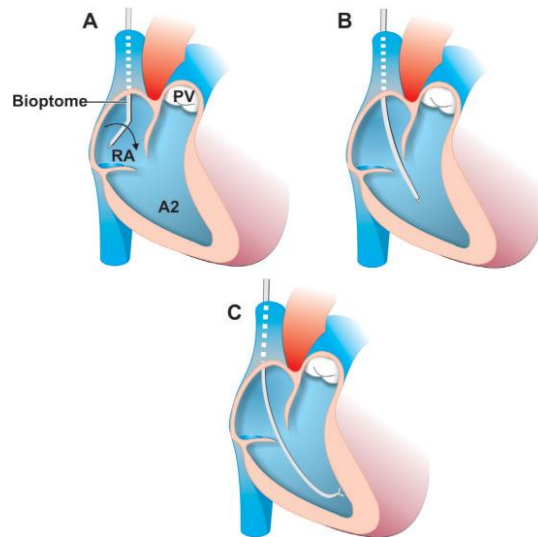
Figure 2.2: Endomyocardial biopsy

A skin biopsy [22] involves the removal of cells or tissue samples from the surface of the body which includes shave biopsy, punch biopsy, incisional biopsy, and excisional biopsy.
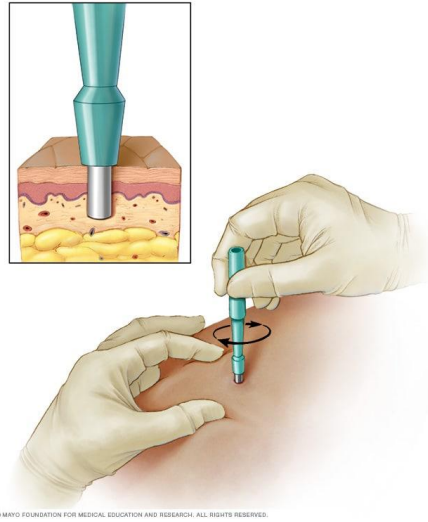
Figure 2.3: Skin punch biopsy

During a bone marrow biopsy, a surgeon retrieves a sample of bone marrow from the back of your hipbone, typically using a long, specialized needle. In specific cases, the sample may be collected from other bones in the patient's body. To minimize discomfort during the procedure, patients typically receive a local anesthetic or other medications.
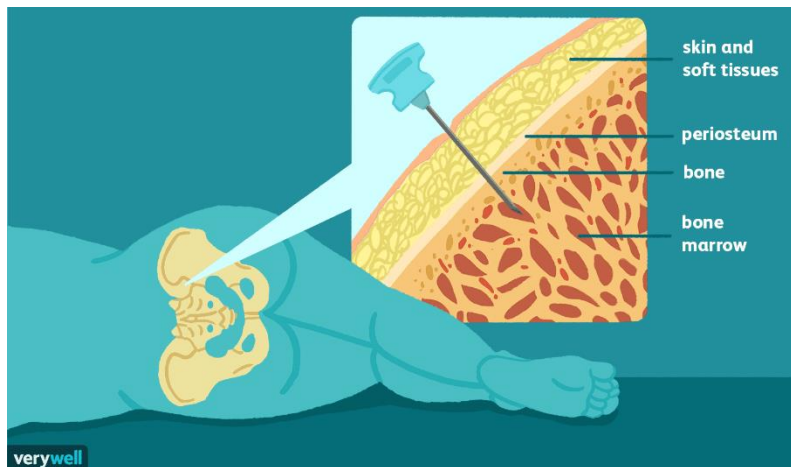
Figure 2.4: Bone marrow biopsy

2.2 Needle Biopsy Procedures and Limitations

Needle biopsies offer several advantages over surgical biopsies. They are minimally invasive, resulting in smaller incisions or no incisions at all, which leads to reduced pain, faster recovery times, and fewer complications. Patients also experience minimal scarring, lower risks of infection, and a quicker return to normal activities. Needle biopsies are more cost-effective, typically require only localized anesthesia, and provide accurate diagnostic results, particularly for conditions like cancer. Their versatility allows for use in various body parts, making them a preferred choice in many clinical scenarios [19].

The process typically involves patient preparation and local anesthesia, followed by precise needle insertion to collect tissue samples. Imaging techniques may be employed for guidance in some cases. Once the samples are collected, they are sent to the laboratory for analysis by pathologists [19].

However, needle biopsy encounters formidable limitations. Central to these limitations is the uncertainty surrounding the incremental benefits of tissue sampling and biopsy procedures. Several factors contribute to this uncertainty. One critical issue is the potential for sampling errors, as biopsies may fail to include the specific affected areas. Additionally, inherent constraints on the amount of target tissue that can be safely biopsied limit the depth of penetration, further complicating the diagnostic process. In response to these limitations, the medical field has explored advanced techniques to enhance diagnostic accuracy with imaging systems including CT, MRI and ultrasonic [26]. Beyond these techniques, researchers also developed disease-specified technique including electroanatomic mapping, cardiac magnetic resonance imaging (CMR), and positron emission tomography. These technologies have been utilized to guide the biopsy process more effectively, enabling the sampling of precisely affected regions. For instance, electroanatomic mapping provides real-time guidance by creating detailed electrical maps of the heart, aiding in pinpointing the areas of interest. CMR [1] offers excellent

10

visualization capabilities, allowing for the identification of myocardial abnormalities. Positron emission tomography provides functional information that can complement structural imaging, contributing to a more comprehensive understanding of cardiac health. While these advanced techniques hold promise in improving the diagnostic accuracy of biopsy, it's important to note that they are not yet widely accessible or routinely performed. Factors such as equipment availability, expertise required for interpretation, and cost constraints may limit their use in clinical practice. As such, efforts should continue to make these advanced diagnostic tools more accessible to clinicians, potentially revolutionizing the way cardiomyopathy and other diseases are diagnosed and treated in a more robust and accurate way.

2.3 Importance in Tissue Classification for Needle Biopsy

In addition, in real-world surgical scenarios, surgeons continue to rely heavily on their intuition and tactile perception of variances in tissue properties while performing manual needle interventions. This intuitive skill allows them to discern anatomical structures and events, such as puncture occurrences and the differentiation between soft and hard tissues. Haptic feedback, derived from the interaction between the needle and the tissue, plays a crucial role in enabling surgeons to make informed decisions during surgical procedures. This intuitive haptic perception is an essential aspect of surgical expertise.

The importance of interaction force in characterizing tissue properties is exemplified in breast cancer diagnosis research [2], where it was found that breast carcinoma has a mean shear stiffness approximately 418% higher than that of surrounding breast tissues. This understanding has led to the development of classifiers that distinguish tissue properties based on force patterns. Research in liver needle insertion, for example, utilizes statistical models to classify tissues by analyzing the force data [3]. Moreover, Young's modulus, a material property indicative of tissue stiffness, can be identified based on the energy stored

11

in the needle-tissue system [4]. Additionally, the application of deep learning, such as a recurrent neural network (RNN) based Long-Short Term Memory (LSTM) model, has shown promise in estimating various synthetic tissue classes [5]. These studies validate the concept that integrating force parameters with position data significantly enhances the comprehension of interactions in a wide range of interventional procedures and diagnostic processes. The collective findings from these studies underscore the critical role of force parameters in surgical interactions. They demonstrate that the integration of force data with positional information improves the understanding of tissue properties, facilitating more accurate tissue classification and diagnostic processes. This integration not only enhances the surgeon's ability to make informed decisions but also holds great potential for automating and advancing medical procedures through intelligent systems, such as the transformer-based method described in your paper. The combination of surgeons' expertise, haptic feedback, and advanced data analysis techniques represents a significant step toward safer and more effective surgical interventions.

2.4 Robotic Biopsy Platforms

Recent developments in the field of robotic biopsy are making significant strides in various disease diagnosis procedures. These advancements excel in enabling precise and accurate needle insertions, greatly enhancing the quality of procedures, especially with the aid of sophisticated imaging systems.

The increasing adoption of minimally invasive procedures, smaller needles, and robotic manipulators is poised to have a transformative impact on patient care. This shift promises to minimize scars and reduce trauma for patients undergoing various medical interventions. Consequently, a new generation of interventional radiologists and surgeons is progressively becoming more adept at utilizing this advanced technology. Regarding the development of biopsy robots, it initially involved modifying industrial robots, which were

characterized by their large size, complexity, and high cost. However, the current trend is moving towards the introduction of smaller, more cost-effective alternatives. These newer robotic systems are designed to be compatible with a wide range of imaging modalities, allowing for versatility in their application across different medical procedures [6].

Robotic biopsy procedures have been deployed across a wide range of anatomical sites, showcasing their versatility and adaptability, such as bone [7], lung [8], breast [9], brain or brainstem [10], prostate [11], and liver [12]. Robotic biopsy's capacity to maintain a straight-line trajectory is particularly valuable, with guidance primarily relying on standard radiological images. In such scenarios, robotic systems serve a dual purpose: they fuse diagnostic and interventional images, and subsequently, they establish a direct path from an external position to the intended target point. These applications demonstrate how robotics enhances precision by seamlessly integrating imaging with precise procedural guidance. These applications also hold the potential to enhance the accessibility and efficiency of robotic-assisted interventions in healthcare.

Commercially available robotic-assisted systems [6] would include: Intuitive Ion system, Perfint Robio, BARD Biopsy Systems, Hansen Sensei Robotic System, etc.

Figure 2.5: Intuitive Ion system

Figure 2.6: Perfint Robio

Figure 2.7: Hansen Sensei Robotic System

Yet, the potential benefits provided by robotic applications within hospital settings, such as improved accuracy, precision, consistent execution of small tasks, enhanced ergonomics, and resistance to fatigue, have not been fully realized. There appears to be a gap between advanced robotic technology and practical clinical needs [6].

2.5 Digital Pathology

For various types of biopsies, the final examination would come to pathology. The traditional practice of pathology has revolved around the examination of stained, thin tissue sections by a trained human using an optical microscope. However, recent technological

advancements are catalyzing significant shifts in this traditional paradigm, ushering in the era of digital pathology (DP) [27]. In its fundamental definition, digital pathology involves the use of computer screens to view scanned histology slides. This approach allows for the digitization of glass slide tissue sections, making it convenient to share these digital images for second opinions and remote consultation. Presently, one of the most widely discussed advancements in the field of digital pathology is the integration of artificial intelligence (AI) for the automatic analysis of tissue images. The novel approach utilizes the physical properties of molecules to extract spatially resolved specific information about the tissue. Label-free vibrational spectroscopic methods, such as infrared (IR) and Raman spectroscopy, play a crucial role in the analysis of these thin tissue sections. This innovative approach holds the potential to revolutionize digital pathology by reducing the reliance on staining and increasing the depth of information obtained from tissue analysis [29].

Among the various techniques used in label-free vibrational spectroscopic methods, the most commonly employed method was Fourier-transform infrared (FTIR) imaging before 2017 [30]. Numerous research groups worldwide have utilized FTIR imaging to initially identify spectral distinctions between different tissue types (both normal and diseased) [31].
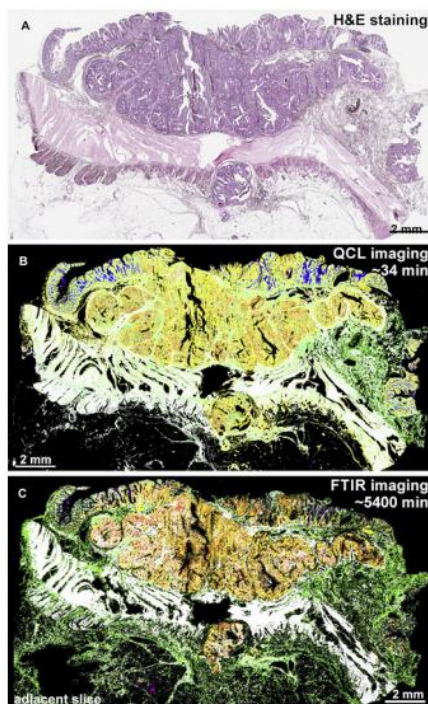
Figure 2.8: Colorectal cancer tissue analysis [31]. (A)H&E staining. (B)Spero QT system. (C)FTIR-based imaging

In recent years, there have been notable advancements in the field of IR imaging systems. These cutting-edge systems have departed from traditional FTIR spectrometers and instead employ quantum cascade lasers (QCLs) as high-power light sources. Notably, research groups led by Bhargava have made groundbreaking discoveries in the realm of chemical imaging by developing their QCL-based microscopes. These innovations represent a significant shift in the technology used for IR imaging and hold great promise for advancing the capabilities of chemical and tissue analysis. This methodology was a crucial milestone in the journey toward potentially integrating label-free digital pathology into clinical practice. This enhanced speed not only facilitates larger-scale studies but also paves the way for label-free digital pathology to align with the established path taken by stain-based digital pathology. This alignment is essential for conducting validation studies and, ultimately, the successful translation of label-free digital pathology into clinical

settings. The ability to scale up and validate this technology is a critical step in its adoption within the healthcare field [28].

2.6 Research Goal

The current limitations in biopsy include low accuracy due to sampling errors, lack of precision and haptic feedback, and the time-consuming nature of staining in traditional pathology.

Our primary focus is on the development of solutions that can provide a rapid and precise platform for robotic biopsies, with a particular emphasis on integration with digital pathology.

To achieve these objectives, the research goal is set to develop a robotic system equipped with a steerable needle-probe that is fully compatible with the state-of-the-art QCL optical fiber technology, enabling specific motion for vibrational spectroscopy. This integration allows for the analysis of tissues' chemical and molecular composition in real-time with the label-free digital pathology.

Additionally, it is also necessary to establish a standardized experimental setup using this robotic system to collect relevant data. This data will be pivotal in training a transformer-based tissue classification model. The primary goal of this model is to enhance the capabilities of surgeons by assisting them in recognizing the tissue environment during needle biopsies.

This technology represents a significant step forward in the field of medical robotics, aiming to improve the accuracy and efficiency of biopsy procedures while leveraging digital pathology for more comprehensive analysis.

CHAPTER 3

FIBER-OPTIC COMPATIBLE ROBOTIC

BIOPSY SYSTEM

3.1 Design and Development of Robotic Biopsy System

3.1.1 Workflow and system overview

The conventional biopsy process has long been a cornerstone of diagnosing various medical conditions, especially cancer. This process involves the extraction of tissue samples from a patient's body after diagnostic testing locates the region of interest, which are then sent to the pathology laboratory. In the lab, these tissue samples are meticulously prepared, sectioned, stained, and analyzed under a microscope by skilled pathologists. This approach, while effective, can be time-consuming and labor-intensive. The proposed method shift in the field of medical robotics represents a significant advancement in diagnostic procedures. As depicted in Figure 3.1(a), instead of the traditional biopsy process, in-situ diagnosis utilizes cutting-edge technology to minimize the need for tissue extraction. After performing initial diagnostic tests to locate the target tissue, the system captures digital image data directly from the patient's body. Virtual images resembling H&E will be taken out in the digital pathology, leading into a fast and accurate digital diagnosing procedures.
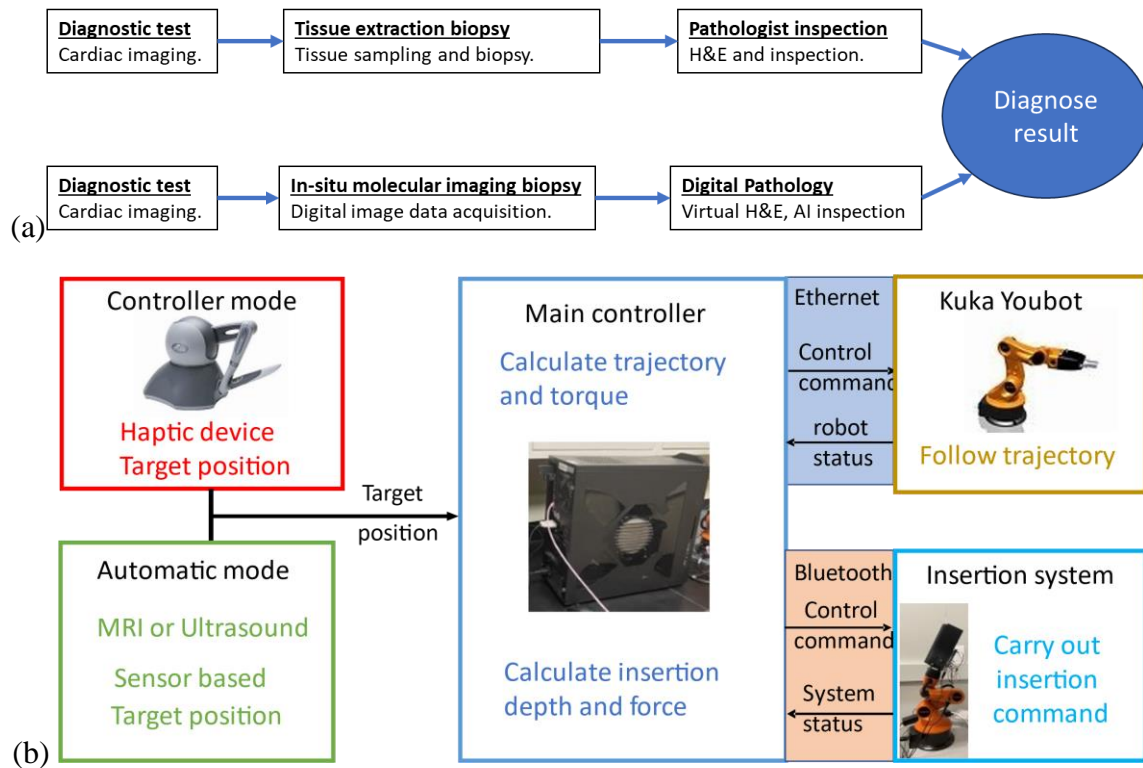
Figure 3.1: Workflow and overview of proposed system. (a) Comparison between conventional method and proposed novel digital approach. (b) Detailed biopsy procedure of our proposed system.

The detailed operation procedure scheme is shown in the Figure 3.1(b). The existing methods like ultrasound can be used to locate areas of interest to biopsy [32-34]. Based on the location within the anatomy of the organ, a unit vector will be determined at the desired location that signifies the establishment of a directional reference within the anatomy [35-37]. This vector serves as a guide, indicating the precise direction in which the probing needle should be inserted. The unit vector calculation is a critical step in ensuring the accuracy and precision of the biopsy procedure. By manipulating the orientation of the probe, it becomes possible to align it precisely with the calculated unit vector. This feature enhances the system capability to target and access specific sites within the anatomy with a high degree of accuracy. The projected needle, once the end-effector head is

19

perpendicular to target tissue, will simultaneously translate and rotate about its axis. The ability to form molecular image patterns is crucial for stainless staining, a technique that can enhance the visualization and characterization of biological tissues.

3.1.2 Mechanical design requirements

The innovative principle of feed-force sensing in the proposed robotic system primarily ensures safety during in-situ needle-probe molecular imaging [38]. Additionally, the system provides a generic steerable platform to incorporate wide knowledge of an intelligence algorithm for tissue detection and estimation using this feed-force parameter. Availing the knowledge of robot navigation and incorporating the mathematical compensation model for needle bending will ensure accurate access to the desired location for in-situ molecular biopsy. The in-situ molecular imaging performed with a steerable end-effector may allow for more optimal image sampling of tissues without removing the tissues from the patient's body. Thus, accurate access to the desired location and molecular imaging sample of large region of the tissue addresses the challenge.

The above considerations lead to the following requirements for the design features: 1). High dexterity with more than six degrees of freedom (DOF) to provide the steerable platform with maneuverability; 2). Strong needle insertion to collect samples from the desired location, which requires at least 20N on the needle [39]; 3). Large and free workspace without a singular point, estimated as a volume of 800 mm (length) * 800 mm (width) * 400 mm (depth) [40], which would further be mapped with haptic control space of the surgeon's operation.

The functionalities of the biopsy system encompass the following: 1). Precisely navigate to the target point with high dexterity; 2). Penetrate the targeted tissue using a 16-gauge biopsy needle and collect a sample from the designated point; 3). Retract the needle and extend the IR scope to the target point; 4). Employ a helical motion to manipulate the infrared scope, obtaining average cytological information from the superficial area

surrounding the target point; 5). retract the IR scope and histologically characterize the extracted tissue with IR imaging for rapid, real-time diagnosis.

3.1.3 Mechanical Design Details

To achieve the goals stated above, we have the following mechanical designs as shown in the Figure 3.2. The mechanical design outlined in Figure 3.2(a) incorporates several key elements that work in tandem to enhance the precision and effectiveness of tissue sampling. The utilization of a five Degrees of Freedom (DOF) Kuka Youbot arm provides a robust and versatile platform for the steerable biopsy system. This robotic arm is capable of precise and coordinated movements in six different directions, offering the necessary dexterity and flexibility to manipulate the biopsy tool effectively. It serves as the primary support structure for the entire system, ensuring accurate motion control and positioning to reach the target tissue. The core of the biopsy system comprises a needle insertion system with three Degrees of Freedom (DOF). This subsystem consists of two essential components: the Standalone Needle Insertion Module and the Pitch Control Unit. This standalone needle insertion module is responsible for the actual insertion of the biopsy needle into the patient's tissue. Its ability to carry out helical motion allows for precise control over the depth and orientation of the needle during the biopsy procedure. This feature is instrumental in ensuring accurate tissue sampling. The pitch control unit plays a critical role in adjusting the insertion angle of the biopsy needle. This adjustability is essential for targeting specific tissue areas within the body. By controlling the pitch, the system can accurately position the needle for biopsy, minimizing the risk of damage to surrounding structures. Figure 3.2(b) illustrates the real-world assembled robotic biopsy system.
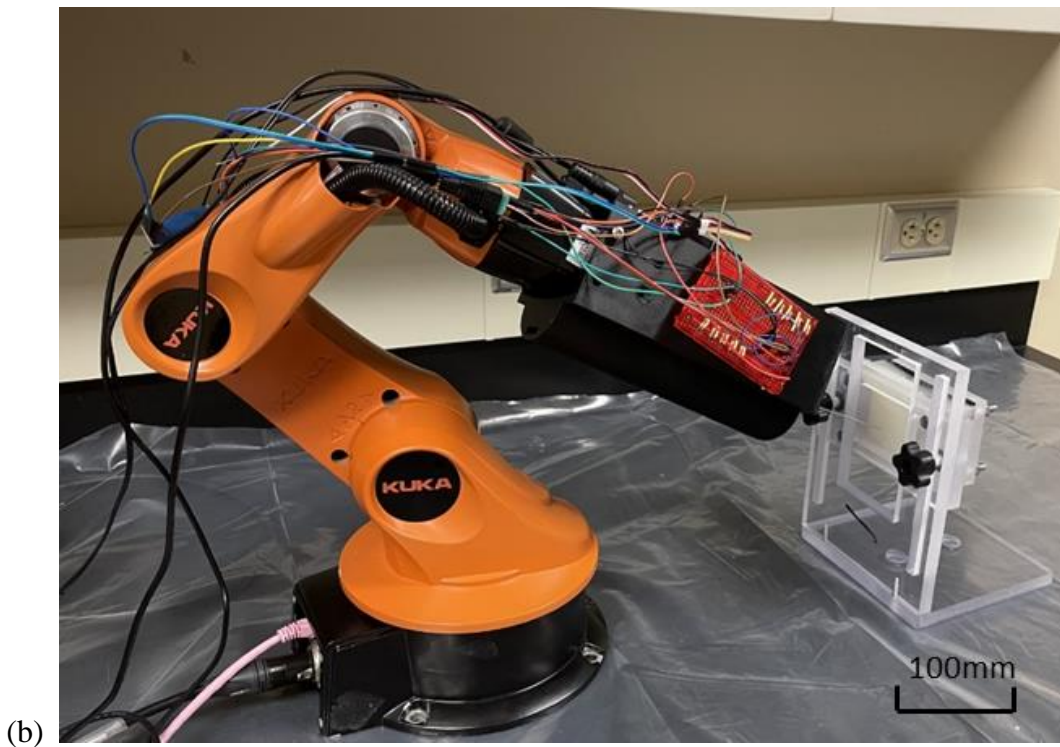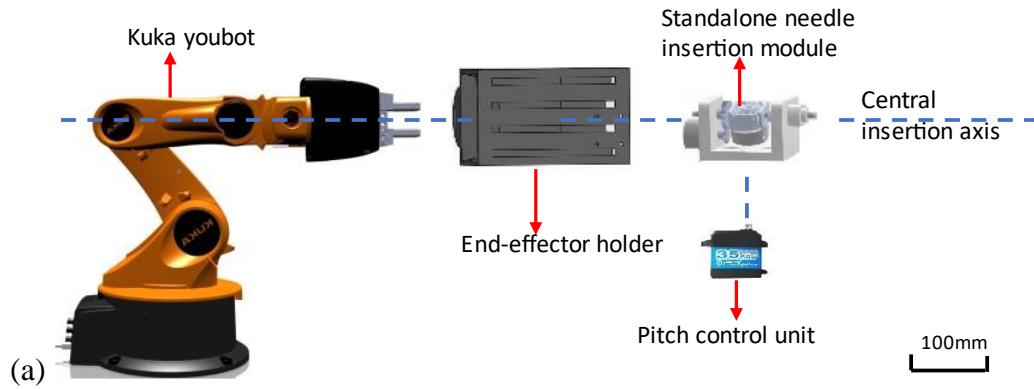
Figure 3.2: Design details of the biopsy system. (a) Mechanical design outlines (b) real-world assembled robotic biopsy system.

To create a cohesive and functional system, the needle insertion system is seamlessly attached to the Kuka robot arm. This integration allows for precise coordination between the two systems. The Kuka robot arm provides the necessary motion control to guide the needle insertion module to the designated target point/tissue, ensuring that the biopsy procedure is carried out with the highest level of accuracy.

Former researchers have designed a standalone module for inserting needles during endovascular procedures [39]. The standalone needle insertion module (shown in Figure 3.3 (a)) is engineered to achieve precise translation and needle rotation at programmable speeds. This capability is essential for controlled and accurate needle insertion during biopsy procedures. It allows for fine adjustments based on user input commands, ensuring that the needle follows the desired trajectory. The central box unit, denoted as BS2, is a critical component of the module. Inside BS2, there are rollers (as depicted in Figure 3.3 (b)) that play a pivotal role in enabling translation along the central insertion axis. These rollers utilize friction wheels to facilitate smooth and controlled movement of the needle. The module employs two actuation mechanisms, m1 and m2, to control translation and rotation, respectively. Actuator m1, attached to BS2, drives the translation motion of the needle along the central axis. Meanwhile, actuator m2 is responsible for rotating BS2 around its axis, thus controlling the rotational motion of the needle. This dual-actuation system ensures precise and coordinated movement during procedures. This module also incorporates a spring-loaded quick release mechanism, which is associated with the passive roller. This mechanism serves multiple purposes. First, it allows surgeons to manually pull the needle in emergency situations, providing a fail-safe option in critical moments. Second, it enables user-defined clamping behavior, accommodating various tool sizes, and allowing customization for different procedural needs. To ensure seamless operation and control of the standalone needle insertion module, the system employs a slip ring for transmitting control signals to and receiving encoder data from actuator m1. This slip ring is akin to the sensor module and plays a pivotal role in facilitating communication between the module and the controller. The description references an exploded view of the standalone needle insertion module, as depicted in Figure 3.3 (c). This view provides a detailed visualization of the module's internal components and their arrangement, offering a clear understanding of how the various parts interact to achieve precise needle insertion.
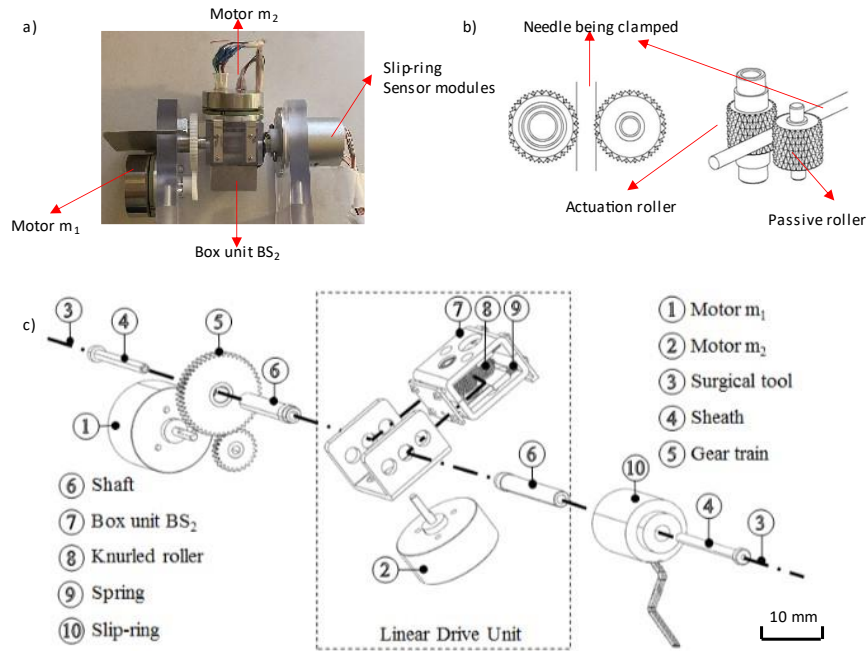
Figure 3.3: Standalone needle insertion module. (a) Design overview. (b) Needle clamping with friction wheels. (c) Standalone needle insertion module exploded view

While the standalone needle insertion module is capable of translation and rotation, needle insertion pitch angle is needed for fine-tuning the insertion axis to avoid unbalanced gyro spinning behavior. Pitch control unit enables the fine axis adjustment while the robotic platform reaches the target position. This also ensures safety concern that undesired needle insertion won't be carried out until the fine-tuning of the insertion axis.

To notice, this standalone insertion module is not only capable of delivering needle, but also optic fiber with various thickness. The spring-loaded mechanism ensures the flexibility in tool dimensions.

Biopsy insertion system has already been developed and tested. Steerable digital biopsy system has been tested on plastic phantom to validate the effectiveness. Validation is discussed in chapter 4.

24

3.2 Compatibility with Label-free Digital Pathology

In the current landscape of label-free digital pathology, label-free vibrational spectroscopic methods, including both infrared (IR) and Raman spectroscopy, are utilized. Of these two methods, IR spectroscopy is more commonly applied in practical use cases. FT-IR spectroscopic imaging is a well-established, high-fidelity technology for histopathologic studies, although it can be slow. The advent of Quantum Cascade Lasers (QCLs) has allowed for DFIR imaging, significantly reducing the time required for histologic imaging. However, it's important to note that cutting-edge QCL applications have primarily been conducted in in-vitro environments. In such setups, a comprehensive arrangement with a movable stage supporting slides, QCL with lenses, microscopes, and other essential equipment are used. These setups enable collected tissues being moved on a slide using the support stage, molecular and chemical images can be recorded using IR vibrational spectroscopy. However, in in-situ situations, it becomes crucial to develop an alternative method for collecting molecular information with a fiber-optic tool inserted directly into the region of interest, as the conventional movement from supporting movable stage is not realistic to collect information across the tissue.

The Figure 3.4(a) demonstrates the acquisition of IR spectral information at one pixel using fiber-optic tools. IR light travels into fiber from QCL, A set of points (marked as green circles in Figure 3.4(a)) at the prism-tissue interface reflect the IR light. Reflected light then travels back to the IR detector thru fiber with information. After IR spectrum analysis, 1 pixel with multi-spectra information is recorded, which includes the combined molecular information from all reflect points. Each pixel is approximately 5μm wide, signifying an exceptionally fine level of detail. However, this pixel only captures information in one certain depth in tissue on the prism-tissue interface. Generally, 1 pixel of information is not sufficient to carry out a comprehensive analysis of histopathological data, so we need a richer source of information for diagnostic and research purposes.

In our biopsy insertion system, we've highlighted the importance of a spring-loaded mechanism that offers flexibility in tool dimensions, making it compatible with fiber-optic tools with different size. As depicted in Figure 3.4(b), the fiber-optic tool is clutched by the two rollers from insertion module. There are 2 driving motors in the insertion module. Fiber optic tool rotates along the insertion axis with motor 1 and feeds straightly under actuation roller driven by motor 2. Multiple pixels are recorded at a certain depth level with rotation, IR change across spectrum domain during rotation, spectroscopic information is recorded. Meanwhile, as the tool feeds straightly into tissue, a sequence of pixels are recorded for different depth. Helical motion has the following benefits in information acquisition:

Firstly, it would gather more information at a certain depth level, allow IR changing across spectrum domain, recording information for multi-spectral IR analysis. Secondly, it has the capability to collect spectroscopic information at different depth, recording enough pixels for a spectroscopic analysis within depth. This helical motion not only minimizes the sampling error by increasing with rich information during the rotation, but also generates a depth analysis so that surgeons can determine the boundary of focal area for further surgical procedures including cutting, removing and other treatments.

(a)

(b)

(c)
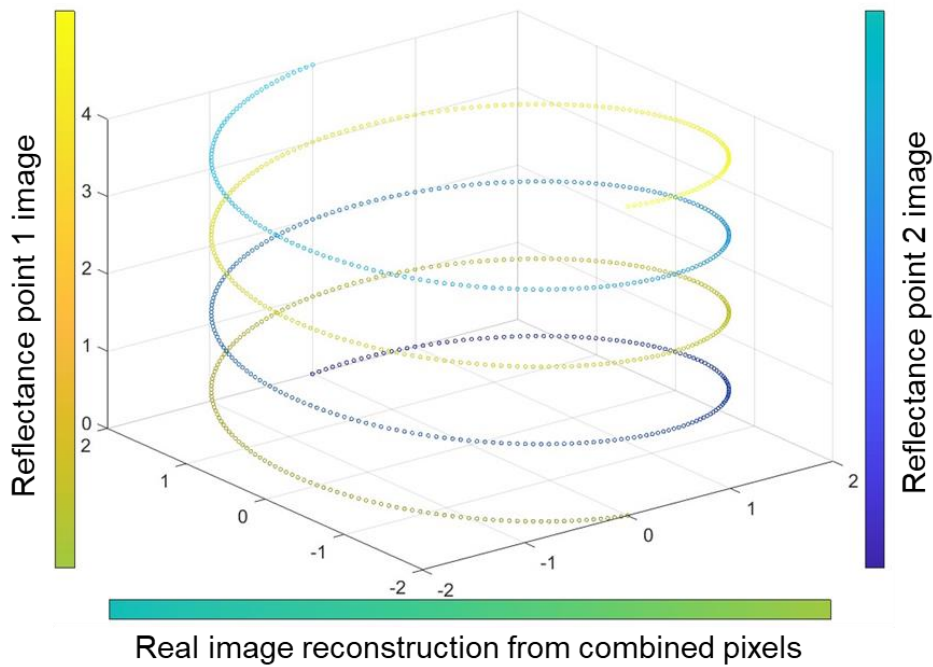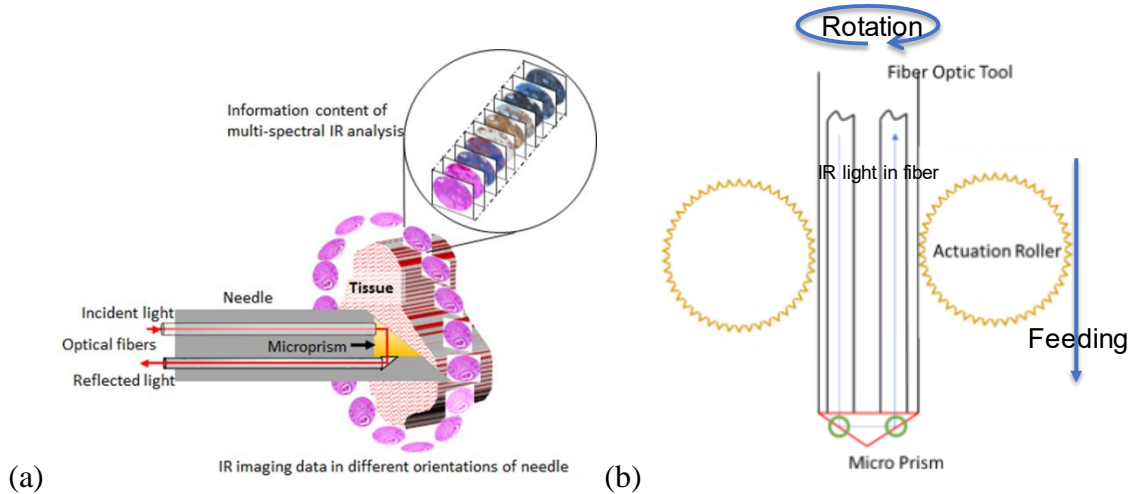
Figure 3.4: Fiber-optic compatibility. (a) IR spectral information at one pixel. (b) Helical motion acquisition. (c) Molecular image reconstruction from reflectance points (unit: mm)

Figure 3.4(c) illustrates the molecular image reconstruction from pixel level during the helical motion. We developed this image reconstruction example for a better understanding of imaging process. To notice, the terms of pixel and image is just a concept here comparing with normal RGB images for better understanding the information combination.

27

Reflectance points on the prism-tissue interface are marked as yellow and blue pixels in helix, represent molecular information recorded in a time sequence. Without losing generality of the concept, we assume 2 points at the prism-tissue interface are reflecting the IR light in this example. The radius of rotation is 2 mm, which is determined by insertion tool and prism size; the feeding depth is set as 2 mm/r, which represents the depth feeds with one complete rotation. The individual spectroscopic reconstructed images for yellow and blue points are demonstrated on the left and right denoted by yellow and blue bars. They are constructed by stacking the pixels from bottom to top, which is indicated by the lightness change in the color bar. However, in a real scenario, it is not feasible to observe their distinct spectroscopic information, as it would be a combined signal as the light travels through the fiber with multiple reflections and we cannot separate the information from 1 reflectance point to the other. Therefore, we would have combined reconstructed images marked as green bar on the bottom, which is the real detected molecular image reconstructed from pixels. Each real collected pixel consists of information from multiple reflections. For instance, the first combined pixel contains information from the bottom yellow and bottom blue reflectance points. The stacking of the combined pixels forms the real molecular image.

3.3 Mathematical Modeling of Robot Kinematics and Workspace

A workspace of 800mm(length) * 800mm(width) * 400mm(depth) general chest biopsy procedures, regarding all kinds of situations and patients' conditions has been reported in the literature [40]. The end-effector shown in Figure 3.5 is designed to have a perpendicular incision angle no matter what posture the patient has. When the robotic arm approaches the target position, the rotational motor inside the end-effector will adjust the needle angle to be perpendicular to the desired position, and the linear actuator will carry out the poking. Figure 3.5 shows the frame of the biopsy system. Corresponding distances between joints

are displayed. The last linear joint from the linear actuator is not shown in the Figure 3.5 since there is always the same safety distance for poking between the joint 5 and desired poking position. Thus, the DH (Denavit-Hartenberg) parameters [41] of the robotic system is shown in the Table 3.1 below:

Joint	a(mm)	α(rad)	d(mm)	θ(rad)
1	0	π/2	L1=33	q1
2	L2=155	0	0	q2
3	L3=135	0	0	q3
4	0	π/2	0	q4
5	0	π/2	L4=170.76	q5
6	L5=120	0	0	q6

Table 3.1: DH parameters for the biopsy system

Since the biopsy system is target-position driven, the inverse kinematics is needed for positioning and workspace analysis.

q6 itself is the pitch joint from the end-effector needle insertion system which makes itself perpendicular to the target position with a safety distance ds, we can transform the target position (x, y, z, φ, θ, ψ) to be (xt, yt, zt, 0, 0, 0) together with the robot base frame. Without loss of generality, we assume the target position to be parallel to the robot base frame, which is (x, y, z, 0, 0, 0).

Since the safety distance ds is a constant, we can get the position of end-effector of the robot as (x, y, z + ds). q1 is the main joint for determining the rotation about its base. Thus, q1 is simply derived as:

$$q1 = \arctan\left(\frac{y}{x}\right)$$
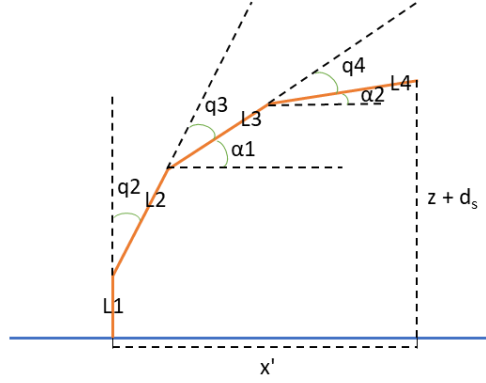
Figure 3.5: Robot representation in (x', z) plane for solving q2, q3 and q4

The remaining q2, q3 and q4 can be derived from the plane (x', z) as shown in Figure 3.5.

$$z + d_s = L1 + L2 \cos q2 + L3 \sin\alpha_1 + L4 \sin\alpha_2$$

With the redundances in planar joints and in order to maximize the working space, we would need to consider with the joints' limit and try to figure out a solution inside the limitation space.

$$\begin{cases} q2 \in (-1.13, 1.57) \\ q3 \in (-2.64, 2.55) \\ q4 \in (-1.78, 1.78) \end{cases}$$

As the limit space of q3 is almost twice as large as q2, and the similar length in arm2 and arm3, we can simply assume the following equation for a large enough workspace.

$$q3 = 2q2$$

put all q2 items to the left of the equations (2) above, square both sides of the equations, add equations together, then we can get,

$$z'^2 + x'^2 + L2^2 + L3^3 - 2(L2\,z'\,cosq2 + L3\,z'\,cos3q2 + L2\,x'\,sinq2 + L2\,x'\,sin3q2) + 2L2L3cos2q2 = L4^2$$

using the equation above and the numerical method, we can get q2 value, and from z' we can get α_2 value, which gives q4 value.

In the context of the system being discussed, the consideration of joint limits plays a pivotal role in defining the maximized workspace. The establishment of a workspace with

30

dimensions of 800 mm x 800 mm x 400 mm holds profound practical implications for the field of medical robotics. As shown in Figure 3.6, the semi-sphere shape workspace can enhance the system versatility, making it applicable to a broader range of medical procedures and interventions. The inner cylinder-shaped space is inaccessible due to the arm length and end-effector length. Joint 1 mechanically limits sweeping angle which causes the left missing part of the semi-sphere. Furthermore, it may allow for the accommodation of various tool sizes and configurations, providing healthcare professionals with a valuable tool for diverse clinical scenarios. Overall, the optimization of the workspace, while considering joint limitations, represents a pivotal step in advancing the capabilities and utility of medical robotic systems, ultimately benefiting both patients and medical practitioners.
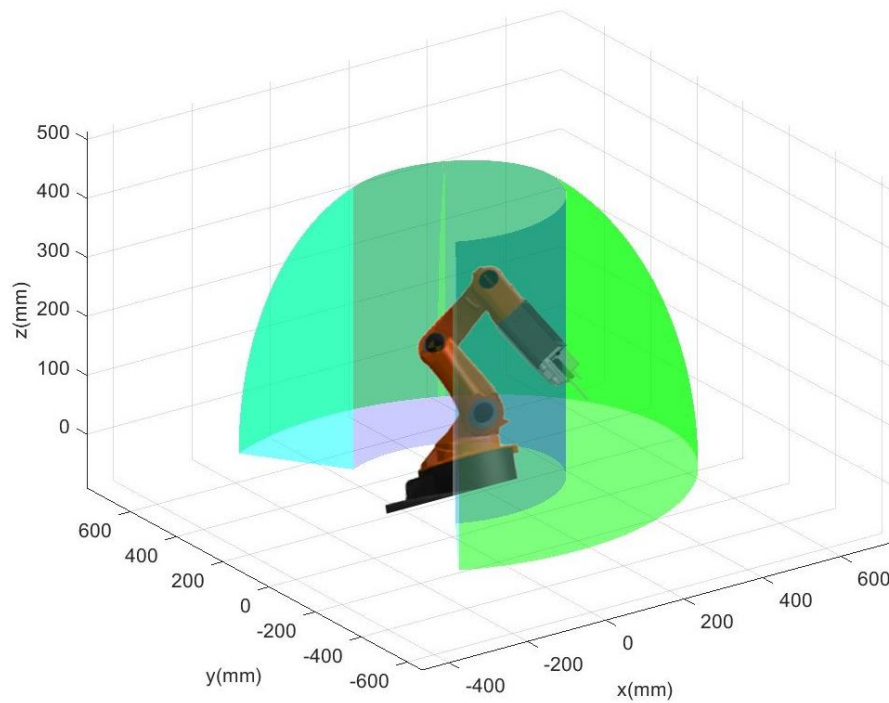
Figure 3.6: Workspace of the biopsy system. (Unit: mm)

3.4 Future Work

We have detailed the design and development of the robotic biopsy system, emphasizing its compatibility with digital pathology, its ability to execute helical motion, and its proficiency in a large workspace. These design aspects have been successfully validated within the robotic biopsy system.

However, it's important to note that the full integration of the current state-of-the-art Quantum Cascade Laser (QCL) technology for developing fiber-based solutions to derive histologic images from molecular data through infrared spectroscopy is yet to be realized. Future research will focus on developing a specific surgical tool that incorporates a tunable QCL spectrometer into a custom infrared (IR) fiber-optic spectrometer. This innovation will mark a significant leap forward in the capabilities of the robotic platform, enabling the generation of histologic images from molecular data.

The current robotic platform continues to concentrate on needle biopsy procedures, prioritizing speed and accuracy in specimen extraction.

CHAPTER 4

SEMI-AUTONOMOUS CONTROL FOR

ROBOTIC SYSTEM

4.1 Control Architecture Overview

The proposed semi-autonomous control for needle incision is illustrated in the block scheme of Figure 4.1. A typical robot-aided needle incision procedure involving the adoption of the proposed control will consist of the following steps:

(1) Robotic platform automatic positioning: With pre-recorded CT/MRI information, the central control processor will generate a planned trajectory to the target location and send real-time control signals to the robotic platform. According to the position/force control algorithm shown in Figure 4.1, the robotic platform will automatically move to the desired location and pose its end-effector aligned with the insertion axis.

(2) Semi-automatic position adjusting: Admittance control is also implemented for the robotic platform. After the automatic positioning, surgeons can activate the semi-automatic adjusting mode. In this mode, robotic platform will react to externally applied force, resorting into a motion control loop. This would benefit surgeons by making larger workspace for multiple tasks besides needle biopsy. This would also fine-tune the target location when the end-effector is not aligned with the desired insertion axis if the patient is not perfectly positioned on an operating table.

(3) Semi-automatic tool insertion: The semi-autonomous control for the tool insertion system is shown in the blue box in Figure 4.1. After the end-effector is aligned with the desired insertion axis, the tool insertion can be performed via teleoperation using haptic

devices. According to the velocity control algorithm shown in Figure 4.1, needle biopsy tool insertion will automatically follow the haptic input, while force feedback will also aid surgeons with information on tissue texture, tool friction, etc.
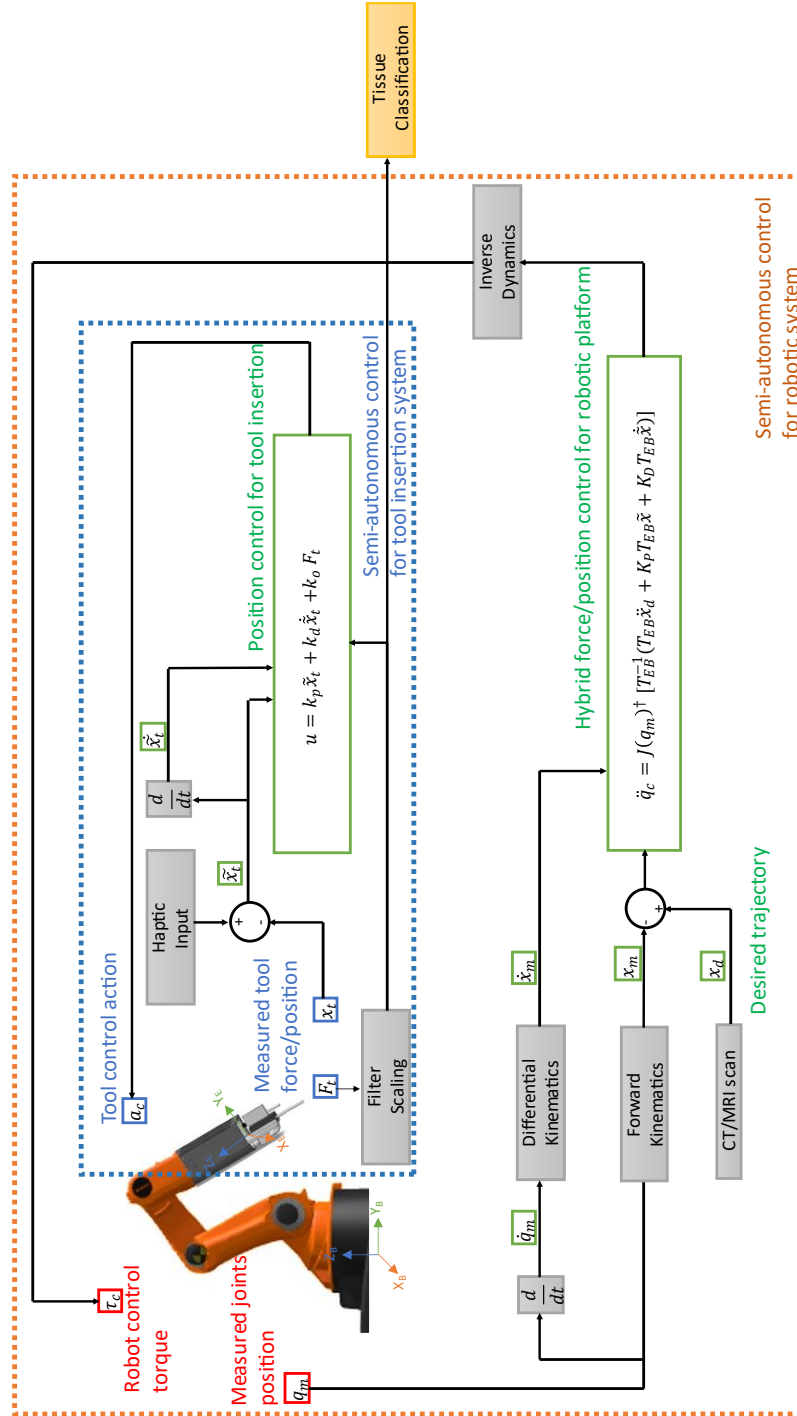
Figure 4.1: Control block diagram of the semi-autonomous control for needle insertion

4.2 Hybrid Force/Position Control

4.2.1 Control Design of the robotic platform

The robotic platform's dynamics and control law are stated as following:

$$\tau_c = M(q)\ddot{q}_c + C(q,\dot{q}) + G(q)$$

$$\ddot{q}_c = J(q)^\dagger \left[T_{EB}^{-1}\left(T_{EB}\ddot{x}_d + K_P\, T_{EB}\tilde{x} + K_D T_{EB}\dot{\tilde{x}} \right) \right]$$

where $M(q)$ represents the inertia matrix of the robot, $C(q,\dot{q})$ denotes the estimation of centrifugal and Coriolis effects, $G(q)$ is the gravity term, τ_c is the computed robotic command torque vector for each joint, $q,\dot{q},\ddot{q}$ represent the robot's joint position, angular velocity and angular acceleration, $J(q)^\dagger$ is the pseudo-inverse of the robot's geometric Jacobian, $\tilde{x} = [\tilde{p},\tilde{\phi}]$ stands for the position error for the end-effector in base reference frame and $\dot{x}_m$ is the robot Cartesian velocity expressed as $\dot{x} = J(q)\dot{q}$ which both are represented in the base reference frame. $\ddot{q}_c$ is the command joint acceleration which is used to compute the joint computed torque. The positioning trajectory from robotic platform initial condition to target position is generated by central processor within pre-recorded MRI/CT image. From this mentioned trajectory, we can get the time-varying x_d and we can calculate $\tilde{x}$ with the subtraction of measured task space position x_m using forward kinematics and the calculated position x_d. $\ddot{x}_d$ is the corresponding acceleration in the generated motion.
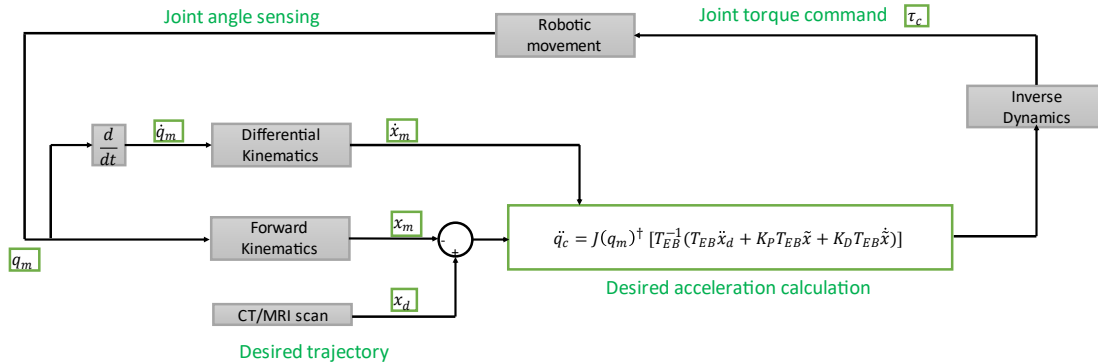
Figure 4.2: Block diagram for robotic platform

Matrix T_{EB} in the transformation matrix which transform the position error $\tilde{x}$ and the velocity error $\dot{x}_m$ from the base frame $[X_B, Y_B, Z_B]$ to the end-effector frame $[X_E, Y_E, Z_E]$.

K_p and K_D are the proportional and derivative control gains that are defined as 6×6 diagonal matrices.

$$K_P = diag\{k_{p1}, k_{p2}, k_{p3}, k_{p4}, k_{p5}, k_{p6}\}$$

$$K_D = diag\{k_{d1}, k_{d2}, k_{d3}, k_{d4}, k_{d5}, k_{d6}\}$$

Using dynamics equation, we get the desired joint command acceleration, and we can then use inverse dynamics used to calculate the commanded joint torques τ_c.

K_p and K_D are tuned for automatic positioning to the desired calculated target position. Under ideal circumstance, the target position where the end-effector will be aligned with the insertion axis would be fixed if the patient does not move. But in real surgical environments, certain moves of the patients' poses or the operation bed heading angle can lead to unalignment of the end-effector to the target insertion axis. Thus, manual operation of fine positioning is needed.

4.2.2 Admittance control for robotic platform

While the ideal scenario envisions the end-effector being perfectly aligned with the insertion axis, the unpredictability of patient movements or changes in the operation bed's heading angle can disrupt this alignment. In response, manual fine positioning becomes a crucial requirement to ensure that the robot maintains its accuracy and precision during surgical procedures. These real-world challenges highlight the need for both admittance control algorithms and hybrid force/position control to handle the dynamic problems and ever-changing conditions encountered in medical settings.

The goal of admittance control is to implement the task-space behavior:

$$F_{ext} = M\ddot{x} + B\dot{x} + Kx$$

where $\ddot{x} \in R^n$ is the task-space configuration in a minimum set of coordinates, M, B, K are the positive-definite virtual mass, damping, and stiffness matrices to be simulated by the system, and F_{ext} is an external force applied to the robot by the operator. The values of M, B, K may change, depending on the location in the virtual environment.

In the admittance-control algorithm shown in Figure 4.3, the force F_{ext} is applied by the operator and can be applied on any links/joints.

For instance, the second link of the robot may contact the operation bed frame, thus the operator needs to pull up that link to avoid collision. With no direct force sensor and variation in force application, it would be very hard to estimate the external force, so we first compensate the friction force in joints, which is represented by $K_f F_f$ term in equation.

And in this case, since no trajectory is strictly followed, we change the equation of dynamics into

$$\tau_c = M(q)\ddot{q}_c + C(q, \dot{q}) + G(q) + K_f F_f$$

$$\ddot{q}_c = J(q)^\dagger \left[T_{EB}^{-1}(K_D T_{EB} \dot{x}_m) \right]$$

where now $\ddot{x}_m, \dot{x}_m$ are measured robot Cartesian acceleration and velocity. We then tune the K_D for gentle motion on the admittance control. And inverse dynamics is used to calculate the commanded joint torques τ_c .
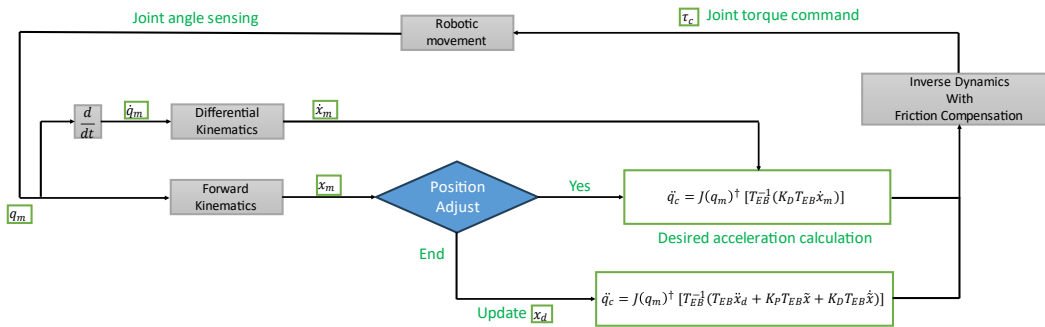
Figure 4.3: Block diagram for robotic platform control with position updates

When the manual adjusting is in process, external force applied on the end-effector will change the desired acceleration, which determine the joint drive torque from joint torque control. When the manual adjusting is finished, the desired location can be updated and desired acceleration calculation can switch back to Hybrid Force/Position Control

The friction force F_f can be modeled as the following:

$$F_f = F_c sgn(\dot{q}) + \beta\dot{q}$$

where F_f is the overall friction force relative to each joint, $\dot{q}$ is the relative angular velocity for each joint, β is the viscous friction coefficient, and F_c is the Coulomb friction and its direction is determined by the relative angular velocity for each joint. System identification is used to parameterize the viscous friction coefficients in the joints.

In the robotic dynamics, K_f will be tuned to have a better performance on friction compensation as a feedforward gain. These adaptations enable the robot to operate in an admittance control mode, where the system responds gently to external forces while maintaining its stability.

4.3 Semi-Autonomous Position Control

End-effector is also semi-autonomous controlled by a surgeon using haptic devices with force feedback. Depending on different physical conditions while tool insertion on patients, the measured resistance force would be different. End-effector should carry out insertion under surgeons' teleoperation with feedback to achieve high precision criteria.

In the semi-autonomous mode, the following control algorithm is introduced in the Figure 4.1 as:

$$u = k_p \tilde{x}_t + k_d \dot{\tilde{x}}_t + k_o F_t$$

where u is the calculated control output, $\tilde{x}_t$ is the position error, calculated by the subtraction of the scaled position x_h from haptic device input and the measured tool

position. $\dot{\tilde{x}}_t$ is the velocity error calculated from position error, providing a reference point for precise control. F_t is the measured force along the insertion axis, reflecting the resistance force encountered during insertion. k_p, k_d, k_o are the tunable control gain factor for position, velocity, and force.

k_p, k_d represent the tunable control gain factors for position and velocity, respectively, ensuring that the end-effector effectively tracks the surgeon's haptic input. Meanwhile, k_o plays a vital role in feedforward control efforts. It compensates for resistance forces encountered during insertion, maintaining precise position tracking despite varying physical conditions. This feedforward control strategy, combining haptic feedback and tunable gains, not only enhances the end-effector's performance but also empowers surgeons with a high degree of control and confidence in achieving exceptional precision during medical procedures.

4.4 Parameters Identification

The detailed mechanical properties of Kuka Youbot can be found in Kuka official website. The mass, max torque and joint limits for arm joints and end-effector unit is measured in Table 4.1.

	joint 1	joint 2	joint 3	joint 4	joint 5	end-effector
mass (kg)	1.39	1.32	0.82	0.77	0.69	1.53
max torque (Nm)	9.50	9.50	6.00	2.00	1.00	/
joint limits (°)	-169°~169°	-65°~90°	-151°~146°	-102°~102°	-165°~165°	/

Table 4.1: Kuka Youbot Parameters

The remaining system parameters that can not be obtained are Coulomb and Viscous frictions on each joint. As the motors are all fixed on the joints, it takes no harm to combine the motor friction with the joint friction as one single term. A good estimation of the

Coulomb and Viscous friction will aid the admittance control performance with higher admittance behavior.

A comprehensive depiction of friction torque in a robot-manipulator joint can be outlined by the Inverse Dynamic Identification Model (IDM) of the robot for actual parameters. The IDM of a rigid robot calculates the motor torques τ_{idm} as a function the motor positions, velocities and accelerations. It is given by the following relation:

$$\tau_{idm} = M(q)\ddot{q} + C(q,\dot{q}) + G(q) + \tau_f$$

$$\tau_f = F_v\dot{q} + F_c \, sign(\dot{q}) + F_T$$

where $q, \dot{q}, \ddot{q}$ represent the robot's joint positions, angular velocities and angular accelerations, $sign(\dot{q})$ represents the sign of joint velocities, $M(q)$ represents the inertia matrix of the robot, $C(q,\dot{q})$ denotes the estimation of centrifugal and Coriolis effects, $G(q)$ is the gravity term. F_v and F_c stand for the diagonal matrix of the viscous and Coulomb friction parameters. F_T is the offset parameter involving temperature and payload terms. Given that the robotic platform operates at a consistent room temperature with minimal fluctuations and the variable component of the load primarily consists of the tissue reaction force (ranging from 0 to 10 N), which is relatively small when compared to the constant elements such as the end-effector mass and robotic mass, it is reasonable to assume that the term F_T remains constant throughout the operations. Therefore, the focus shifts to identifying and quantifying the components F_v and F_c to complete the friction model.

The most prevalent approach for estimating friction torque in robot-manipulator joints involves isolating it by utilizing measurable control torque. This separation process takes into account the contributions from the other components in the equation above, while considering the mass-inertial characteristics of the robot's links, and subsequently eliminates those contributions. This approach involves paired counter-directed motions performed by one robot axis at a constant velocity ($\dot{q}$ const) with no external load. The constant speed ensures that there is no influence of inertia forces, with centrifugal and

Coriolis forces directed radially from the considered joint, creating torque that only affects subsequent joints and links. Consequently, based on the dynamic equation, the components of inertia forces $M(q)\ddot{q}$ and those of centrifugal and Coriolis forces $C(q,\dot{q})$ are both 0, while the axial control torque u opposes only the friction forces τ. It's important to note that the gravitational component of the load torque lg(θ) is independent of the motion direction $sign(\dot{q})$, while the friction torque component τ changes sign when the direction is reversed. Thus we can denote the positive direction motion torque and negative direction motion torque as $\tau_{idm}{}^{+}$ and $\tau_{idm}{}^{-}$, and the friction torque can be derived as:

$$\tau_f = \frac{\tau_{idm}{}^{+} - \tau_{idm}{}^{-}}{2}$$

The parametrization of a model is considered optimal when it minimizes the Mean Squared Error (MSE) between the vector of measurements. Linear regression using gradient descent is used to optimize the result. The following Table 4.2 shows the result for friction identification.

	joint 1	joint 2	joint 3	joint 4	joint 5
Fc(Nm)	0.504	0.217	0.134	0.113	0.288
Fv(Nms/rad)	0.112	0.076	0.058	0.043	0.085

Table 4.2: Kuka Youbot Friction Identification

4.5 Performance and Safety Evaluation

4.5.1 Evaluation on hybrid force/position control experiment and results for robotic platform

Evaluating the performance of a robotic platform is a critical aspect of ensuring its reliability and effectiveness in medical procedures. To comprehensively assess the

capabilities of the hybrid force/position control system, a series of pre-calculated trajectories are employed for evaluation purposes.

The first set of trajectories involves sine waves executed separately along the $[X_E, Y_E, Z_E]$ axes. Each axis within the target space follows a distinct sine wave pattern, featuring an amplitude of 0.05 meters, while the remaining axes and end-effector pointing direction remain constant. This approach enables a detailed examination of how the robotic platform responds to sinusoidal motion in each specific direction.

The desired trajectories and actual trajectories are shown in the following Figure 4.4(a):
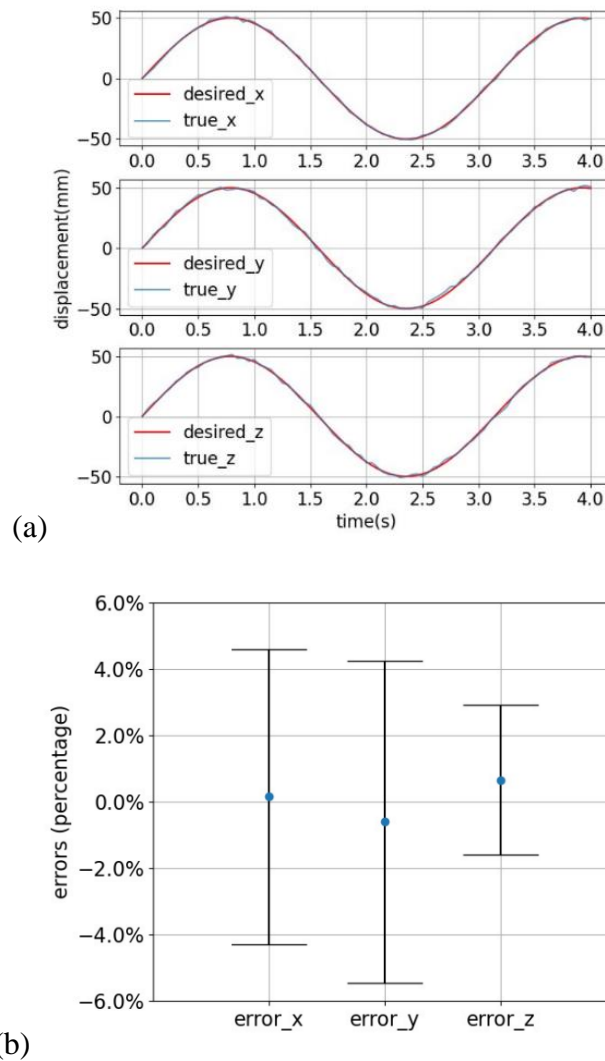

(a)

(b)

Figure 4.4: Hybrid force/position control evaluation (a) trajectory tracking in three axes.

(b) trajectory tracking errors.

42

The quantitative evaluation of tracking performance reveals even more about the system capabilities. As shown in Figure 4.4(b), with mean errors in $[X_E, Y_E, Z_E]$ tracking measuring less than 1 millimeter, and a standard error of tracking below 6% (around 3 millimeters), these results provide concrete evidence of the system consistent and reliable performance. These tight error margins indicate that the hybrid force/position control loop excels in maintaining trajectory fidelity, even when executing separate trajectory waves along distinct axes. Errors measuring in millimeters or less underscore the potential for safer and more accurate surgical procedures. This level of control and reliability has the potential to redefine the possibilities in minimally invasive surgeries, patient safety, and overall surgical efficiency. The success in achieving a well-controlled separate trajectory following in $[X_E, Y_E, Z_E]$ reinforces the immense promise and potential of the hybrid force/position control system in advancing the field of medical robotics to new heights of precision and effectiveness.

4.5.2 Admittance control experiment and evaluation with safety

A comprehensive evaluation of the hybrid force/position control system for the robotic platform is a pivotal step in assessing its overall performance and versatility. To this end, a series of different pre-calculated trajectories have been meticulously designed for systematic evaluations. These evaluations are instrumental in gauging the system ability to adapt to various scenarios and challenges encountered in real-world medical procedures. The results derived from these assessments provide valuable insights into the system precision and robustness, ultimately contributing to its refinement and optimization.

For trajectory evaluations, the performance of the admittance control component within the robotic platform is subjected to rigorous assessment. This assessment involves manual fine positioning after the platform has reached its desired position. This human-in-the-loop approach enables an in-depth evaluation of the system responsiveness and precision when

fine adjustments are necessary. By simulating real-world scenarios where surgeons may need to make adjustments during a procedure, the platform's reliability and effectiveness can be thoroughly examined.

Figure 4.5(a) provides a visual representation of the results obtained from the assessments of the end-effector's response when subjected to external forces. This visualization is essential for gaining insights into how the admittance control system interacts with the hand adjustment while adhering to the preset trajectory. It illustrates the platform's ability to adapt and align its end-effector with the desired trajectory while accommodating external forces, highlighting the system precision and adaptability. Complementing the end-effector's motion, Figure 4.5(b) offers a detailed view of the corresponding robotic joint torque responses when confronted with resistance forces. This analysis reveals how the robotic platform reacts to external forces by generating appropriate joint torques. This response mechanism ensures that the platform maintains its intended trajectory and achieves precise positioning even when faced with varying external forces. The joint torque analysis provides quantitative evidence of the system robustness and its ability to handle real-world challenges effectively. Following the manual operation and fine positioning, the robotic platform's ability to record the final destination and maintain a stable position is a significant accomplishment. This feature ensures that once the manual adjustments are completed, the platform holds its position securely. This capability is crucial in surgical contexts where stability and accuracy are paramount. By achieving a stable final position, the robotic platform contributes to the overall success and safety of medical procedures, aligning with the high precision standards required in the field of medical robotics.
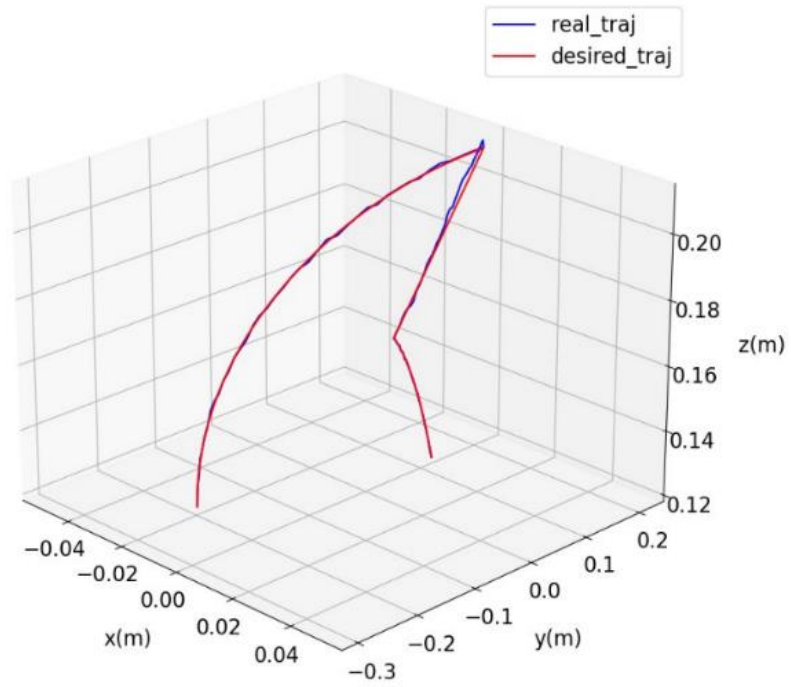
(a)
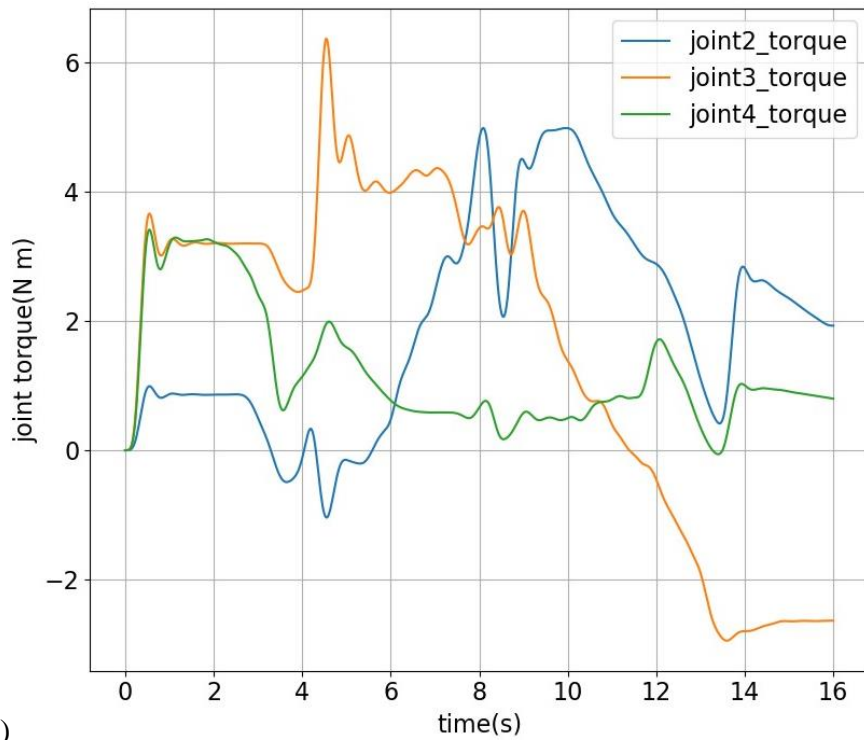
(b)

Figure 4.5: Admittance control evaluation. (a) trajectory tracking with manual positioning for admittance control. (b) torque response for admittance control

4.5.3 Position control and force measurement for tool insertion

To comprehensively assess the performance of the position control system for tool insertion, a thorough evaluation has been conducted. This evaluation involves both position tracking and the measurement of tissue reaction forces under different load conditions, providing a comprehensive understanding of the system functionality and robustness. The experimental setup, as illustrated in Figure 4.6, serves as the foundation for this evaluation. It simulates the real-world needle insertion process, where both the robotic positioning platform and the tool insertion system work in concert. The objective is to measure the position-tracking accuracy along predefined trajectories and simultaneously capture the corresponding tissue reaction forces. This setup facilitates a controlled and systematic assessment of the system performance.

(a)   (b)
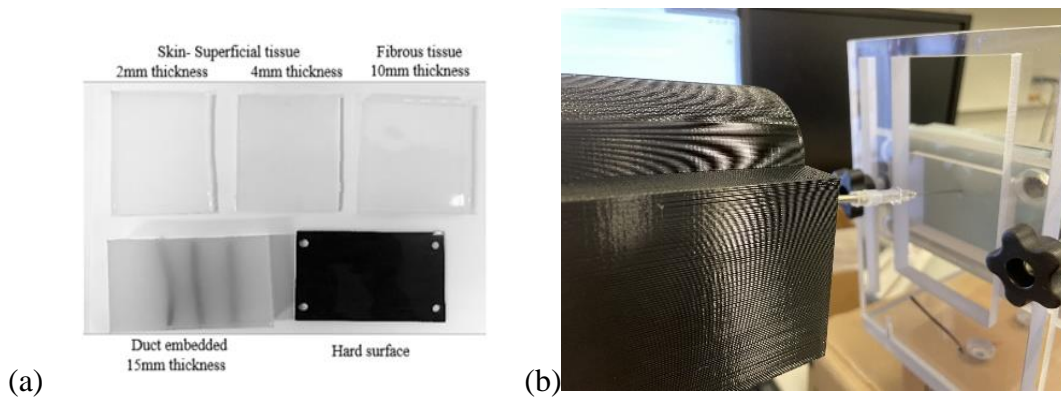
Figure 4.6: Tool control evaluation setups. (a) synthetic tissue sample setups (b) experimental setup for position control and force measurement for needle insertion

For precisely measuring position tracking with certain trajectory and the corresponding tissue reaction force, the biopsy system with 3 DOF (shown in Figure 4.6 (b)) consists a potentiometric position sensor (IR robot: IR-10kΩ linearity potentiometer), a force measurement sensor (ATI model: Nano 43 Transducer), a biopsy cut needle (Bard instrument: 16-gauge/1.7mm). These components work in tandem to replicate the conditions encountered during actual medical procedures, enabling a comprehensive assessment of the system performance in a controlled laboratory environment.

In the evaluation process, a set of synthetic tissue samples with varying types and thicknesses is introduced, as depicted in Figure 4.6(a). These synthetic tissue samples serve as critical test subjects, simulating the diversity of tissue conditions encountered in real medical scenarios. The inclusion of different tissue types and thicknesses enhances the realism of the evaluation and ensures that the system performance is rigorously tested across various tissue profiles. To facilitate the evaluation, the robotic platform and corresponding supporting frames are employed, as illustrated in Figure 4.6(b). These frames are designed to securely hold the synthetic tissue samples in precise positions during testing. Their role is instrumental in replicating the stable positioning required for medical procedures and ensuring that the evaluation accurately simulates real-world conditions.

The evaluation encompasses a range of synthetic tissue sample setups, each designed to emulate distinct medical scenarios.:

1. 2mm skin-superficial tissue + 15mm duct embedded tissue.

2. 2mm skin-superficial tissue + 10mm fibrous tissue.

3. 4mm skin-superficial tissue + 15mm duct embedded tissue.

4. 4mm skin-superficial tissue + 10mm fibrous tissue.

To conduct the evaluation, a continuous input signal of 2mm/s is commanded for needle positioning. This controlled input rate ensures consistency in testing conditions which also mimics the real scenarios in surgical procedures. Relative force feedback and position responses are recorded throughout the evaluation process.

(a)

(b)   (c)
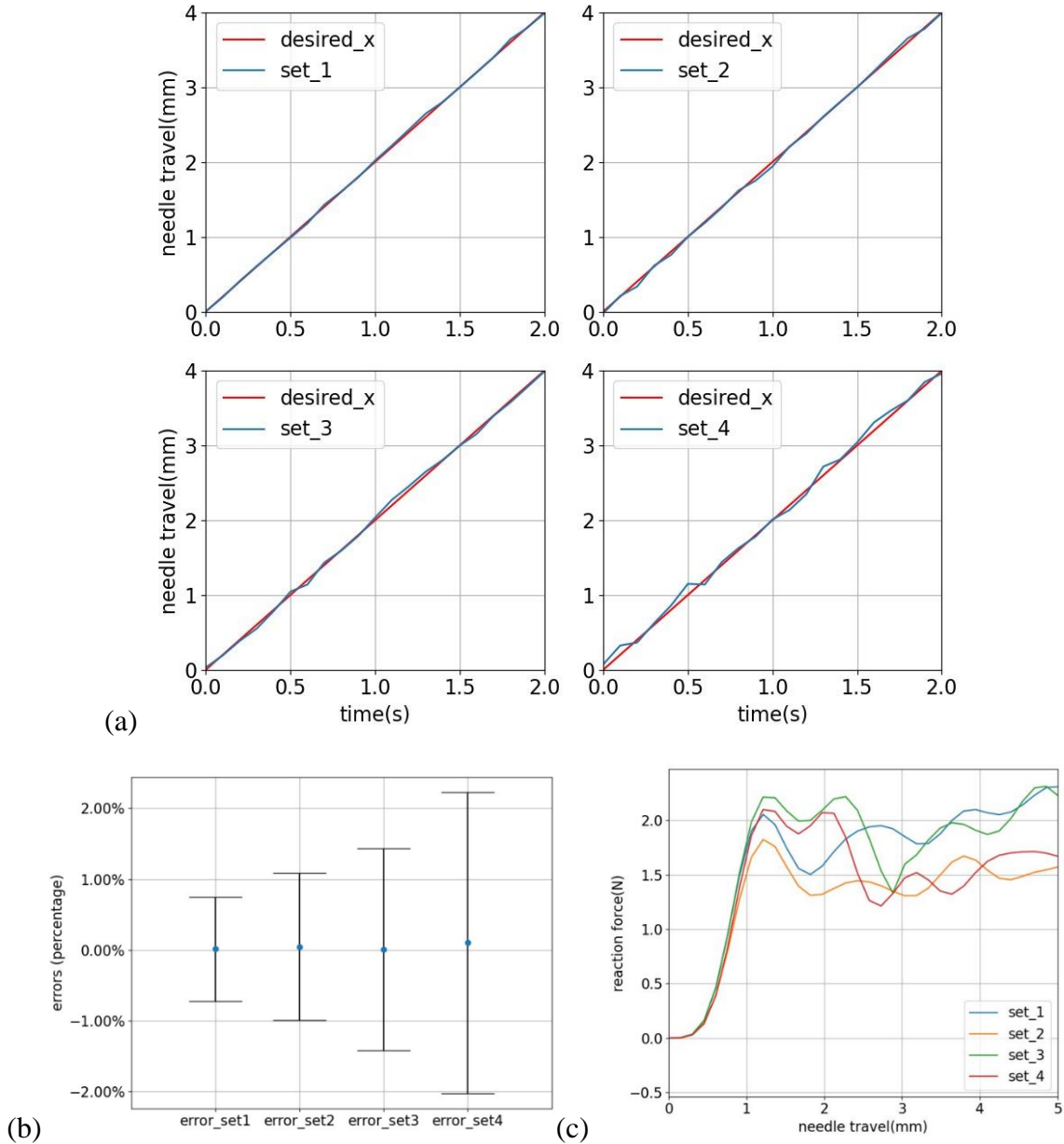
Figure 4.7: Tool insertion evaluation. (a) trajectory tracking for different tissue sets. (b) trajectory tracking errors for different tissue sets. (c) tissue reaction forces for different tissue sets with respect to needle feeding depth

Figure 4.7(a) presents an insightful overview of the position tracking performance in response to the reference signal. The tracking behavior is systematically displayed for four distinct scenarios involving different synthetic tissue setups, each represented by a unique color code. This visualization allows for a direct comparison of the platform's response

48

across various tissue conditions, providing a clear assessment of its precision and adaptability during needle tool insertion. Figure 4.7(b) offers a comprehensive analysis of relative tracking errors associated with the different synthetic tissue setups. These tracking errors are a critical metric for evaluating the system accuracy and reliability. Notably, the mean and standard error of tracking errors measuring less than 1mm underscore the system exceptional precision and robust tracking behavior. This level of accuracy is paramount in medical applications where precise positioning is essential for patient safety and successful procedures. Figure 4.7(c) delves into the corresponding tissue reaction forces observed in various synthetic tissue setups. These forces are indicative of how the system interacts with different tissue compositions and thicknesses during the insertion process. The evaluation of different tissue setups reveals distinct penetration points during the needle insertion process. For both set1 and set2 scenarios, penetration occurs at approximately 4mm of travel. Similarly, for set3 and set4 scenarios, penetration is observed around the 4mm mark. These penetration points provide critical insights into how the system interacts with different tissue compositions and thicknesses during insertion. The evaluation further highlights variations in resistance forces based on the specific tissue setups. In scenarios like set1 and set3, characterized by stronger elasticity in fibrous tissue, the resistance forces encountered during insertion are notably stronger compared to the resistance observed in duct tissue for set2 and set4. This divergence in resistance forces underscores the system ability to adapt to tissue-specific properties, emphasizing the importance of understanding tissue behavior in medical robotics. This multifaceted evaluation offers a comprehensive understanding of the system performance in response to varying tissue conditions, reinforcing its potential for medical applications.

4.6 Conclusion

In chapters 3 and 4, a steerable needle-probe biopsy system is presented. The proposed design achieves high dexterity to provide the steerable platform with accurate access to the desired location, carries out strong and rapid poking to collect samples from the desired location, and provides with large and free workspace without a singular point.

The innovative mechanical design of the steerable needle probe end-effector is discussed in chapter 3. A 5 DOF Kuka Youbot arm is used to support the 3 DOF needle insertion system and provide motion to target point/tissue. A needle insertion system with 3 DOF is consist of a standalone needle insertion module and a pitch control unit. The needle insertion module can carry out helical motion while the insertion angle can be adjusted by the pitch control unit.

To achieve the required high dexterity, we introduce semi-autonomous control for needle insertion in chapter 4. A position/force control algorithm automatically maneuvers the robotic platform to the desired location while aligning the end-effector with the insertion axis. Admittance control is also integrated into the system, allowing the robotic platform to make fine adjustments to the target location when the end-effector isn't perfectly aligned with the desired insertion axis, particularly when the patient's positioning is not ideal on the operating table. The semi-autonomous control loop is also discussed for tool insertion system. After the end-effector is aligned with the desired insertion axis, the tool insertion can be performed via teleoperation under user haptic device inputs or preset insertion behavior.

Chapter 4 also includes an evaluation of the control system. Implemented trajectories are executed using the position/force control algorithm, and the relatively low positioning errors validate the precision of the robotic platform control. Functionality for admittance control is also validated, a user-customized trajectory is achieved with the robotic resistance force rejection. Finally, the overall functioning of position control for tool

insertion is tested. Synthetic tissue samples with different types and thickness are penetrated. Meanwhile, position tracking error is relatively small and reaction force is well recorded and can be transferred to haptic devices for haptic feedback to aid surgeon with information of tissue texture, tool friction, etc.

Safety is also a significant consideration in this context. The admittance control allows for precise manual positioning and adjustments, especially when the needle insertion axis is not perfectly aligned with the desired axis. The precision in position tracking ensures the safety of the robotic platform when performing various tasks. In the application of digital pathology with fiber insertion, maintaining the feeding speed of the end-effector is crucial.

In addition to the content illustrated in this paper, needle insertion is conducted with the assumption of being fully aware of the target position. In real surgical situations, even with pre-recorded CT/MRI scans and ultrasonic guidance, accurately locating the target position of interest can be challenging. In our ongoing research, we are exploring methods to improve the accuracy of needle insertion. This includes investigating techniques such as deep learning based on tissue feedback forces to determine target tissue properties. The potential advantages of integrating machine learning or reinforcement learning with tissue feedback force analysis hold great promise, and we expect these developments to significantly enhance the accuracy and efficiency of our steerable needle-probe system. All these lead to the research presented in chapter 5 of integrating the recognition of tissue properties with the depth of insertion and interaction force. This innovative approach aims to guide the steerable needle more effectively to the target point within tissues or muscles, all while minimizing excessive insertion to mitigate potential side effects.

CHAPTER 5

TISSUE CLASSIFICATION FOR BIOPSY

USING TRANSFORMER MODEL

The current limitations in biopsy encompass low accuracy attributed to sampling errors and a deficiency in precision and haptic feedback. Therefore, the implementation of haptic-based feedback is imperative to facilitate surgeons or operators in better understanding of the environment, especially when dealing with low-fidelity systems. An established standardized experimental setup, as introduced with the robotic system above, has been put in place to gather pertinent data. This data will play a pivotal role in training a transformer-based tissue classification model. The primary objective of this model is to augment the capabilities of surgeons by assisting them in recognizing the tissue environment during needle biopsies.

5.1 Modeling of Mechanics in Needle-Tissue Interaction

As our research aims to detect transitions between different types of tissues, we need to formalize a mechanical model to describe the transitions happening during needle-tissue interactions based on needle insertion force. The interactions between needles and soft tissues have been thoroughly examined and modeled by numerous researchers in the context of various medical procedures [44]. A survey conducted in 2022 [45] highlights that researchers have made advancements in various aspects of needle-related analysis.

These advancements encompass the modeling of cutting forces during insertion, the study of tissue material deformation, the analysis of needle deflection throughout the needle insertion process, and the development of robot-controlled insertion procedures. An influential paper [46] provided insight into the modeling of needle insertion forces when applied to bovine liver tissue. This study effectively characterized the insertion process into three distinct phases, with the puncture of the tissue capsule marking a key transition point.

The insertion force is a summation of stiffness, friction and cutting force:

$$f_{needle}(x) = f_{stiffness}(x) + f_{friction}(x) + f_{cutting}(x)$$

where x stands for the insertion distance. The stiffness force occurs before the puncture of the surface, and the friction and cutting forces occur after this main puncture. Stiffness is best fit by a second-order polynomial of the form, friction force is modelled by modified Karnopp model, and cutting force is considered as constant for a given tissue. This research marks the key transition point at the puncture event and divides the insertion process into three distinct phases: pre-puncture, puncturing, and post-puncture.

For our model of needle-tissue interaction, we consider using Okamura, A.M.'s method for separating the insertion process into three distinct phases. Figure 5.1(a) illustrates the collected data samples within this insertion phase model. In the pre-puncture phase, needle interaction force is dominated by stiffness force and increases within depth. In the puncture phase, as the needle pierces the surface, stiffness suddenly drops and cutting force is taken into account after a short period. In the post-puncture phase, friction force becomes evident, and when combined with the stationary cutting force, it results in an overall increase in the needle interaction force as the needle travels deeper.
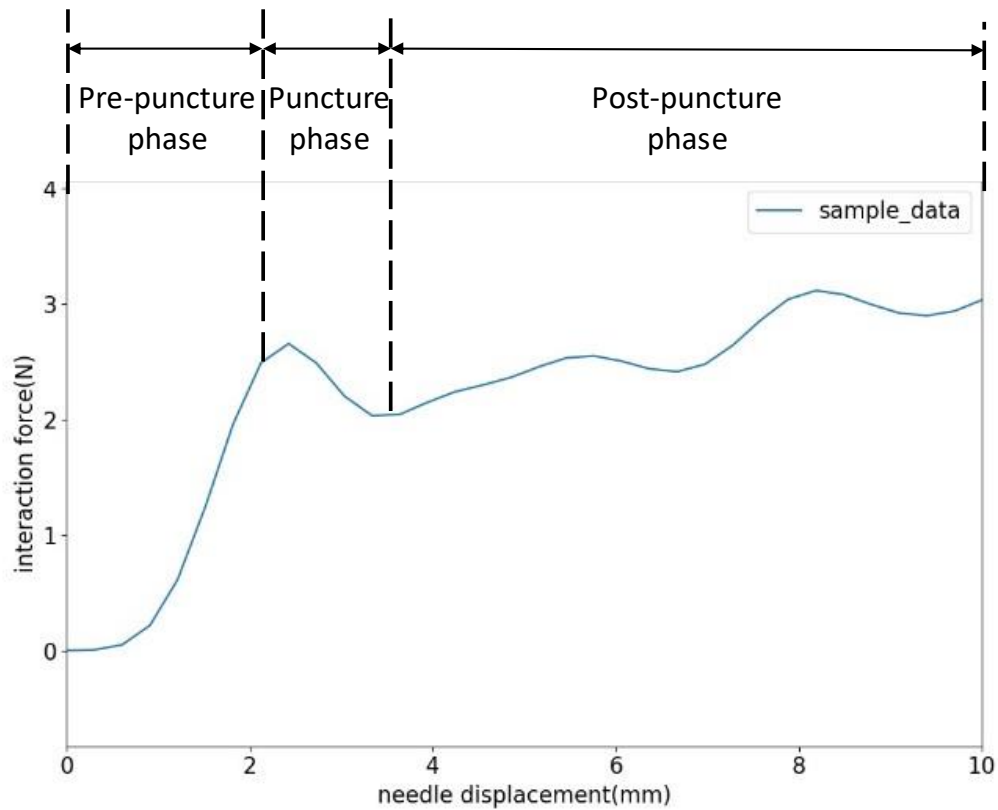
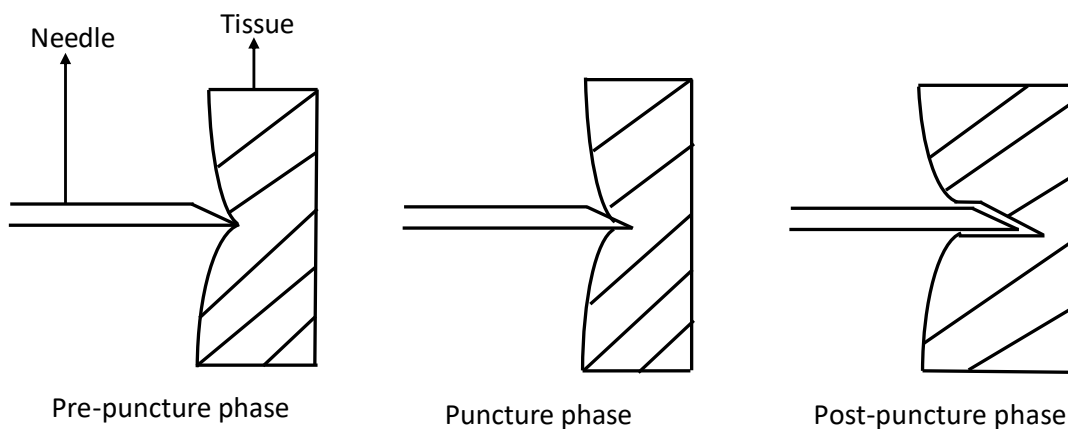Figure 5.1: Needle insertion phase model (a) Needle insertion phase on a sample data

frame (b) Conceptual drawing of phase change

Figure 5.1(b) offers a conceptual illustration that visually illustrates the phase transitions

occurring before, during, and after the puncture takes place. Each drawing in the sequence

features the insertion needle represented by the thin object on the left, and the target tissue

represented by the solid block object on the right. During the pre-puncture phase, there is no penetration, and tissue deformation occurs primarily due to stiffness. In the puncture phase, the needle pierces the surface, resulting in a partial cut into the tissue. Finally, in the post-puncture phase, the needle is fully inserted into the tissue, with both friction force and cutting force being applied to the needle.

The introduced mechanical model would be a baseline for labeling the collected tissue data frame.

5.2 Transformer Model for Classification and Prediction

While the analytical model for needle insertion force depending on phases is convincing, the complexities arising from variations in human anatomy, biomechanical properties, physiology, and geometry make the modeling process intricate and challenging to quantify. To enhance model accuracy, the Finite Element Method (FEM) is employed to simulate tissue deformation during needle insertion and analyze the interaction force [46]. FEM is precise when modeling small, linear elastic deformations. However, FEM calculations can be time-consuming, and the accuracy of FEM is highly reliant on the quality of its inputs.

In the context of these intricate modeling challenges, as an alternative to deterministic modeling, researchers have explored the application of stochastic machine learning techniques to assess the feasibility of comprehending needle-tissue interactions. A dichotomizer Bayesian classifier [3] was used to detect hepatic tissue and vein. A recurrent neural network (RNN) based Long-Short Term Memory (LSTM) model was trained to estimate the various synthetic tissue classes [5].

In recent years, the transformer model has garnered significant attention owing to its robust temporal modeling capabilities. It has found successful applications in diverse domains such as speech recognition [47] and computer vision [48]. The key innovation of the transformer model lies in its self-attention mechanism, which facilitates interactions

among data points in the input sequence by computing similarity scores (attention weights) among them [49]. Furthermore, in comparison to recurrent neural networks (RNNs) like LSTM, which possess similar global context aggregation capabilities, transformers offer the advantage of parallel computation [50]. Transformers provide more efficient processing and improved performance in many time-series processing.

In order to classify our subjective of event detection of tissue transitions, we developed the following transformer-based model:
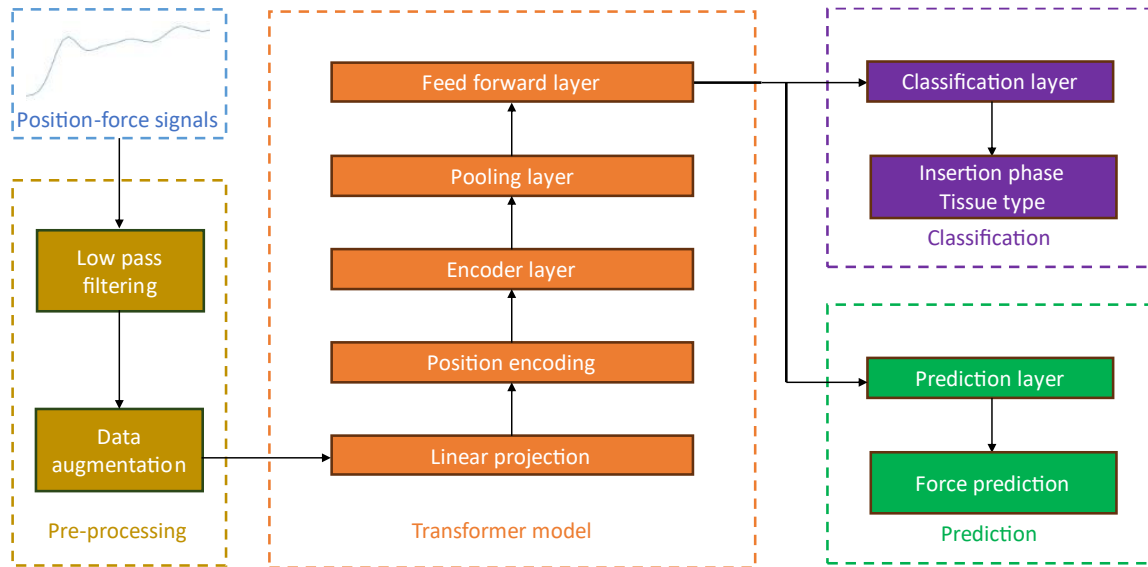
Figure 5.2: Model architecture for classification and prediction

The model architecture is depicted in Figure 5.2. It begins with the collection of position-force signals from various needle-tissue insertion experiments. These raw signals subsequently undergo a low-pass filter to eliminate high-frequency noise [51]. Data augmentation techniques are then applied to enrich the dataset. The processed position-force signals pass through linear projection and position encoding [52] steps to generate the necessary inputs for the transformer. Encoder layer [53] is then employed to extract relevant features. A pooling layer [54] is introduced to reduce the spatial dimensions of the output volume. Following this, a feed-forward layer, also known as a Multilayer Perceptron

[55], is applied to either classify or regress complex data. After the transformer architecture, either classification or prediction tasks are carried out. In the classification module, a softmax classification layer [56] is implemented to determine the insertion phase and tissue types with corresponding labels. Prediction module will be illustrated in the following section.

The encoder layers are shown in detail in Figure 5.3. The encoder block, denoted within the blue box, employs the self-attention mechanism to enhance each token (embedding vector) by incorporating contextual information from the entire time series. Given the context provided by surrounding tokens, each token can have multiple semantic and functional associations. To address this, the self-attention mechanism [57] employs multiple heads, allowing for eight parallel attention calculations. This enables the model to access different embedding subspaces. The position-wise feed-forward network (FFN) within the encoder block consists of a linear layer, ReLU activation, and another linear layer [58]. It processes each embedding vector independently using identical weights. Thus, each embedding vector (with contextual information from the multi-head attention) goes through the position-wise feed-forward layer for further transformation. Residual connections ensure that previous embeddings are carried forward to subsequent layers [59]. This mechanism allows the encoder blocks to enrich the embedding vectors with additional information acquired from multi-head self-attention calculations and position-wise feed-forward networks. Multiple stacked encoder blocks are used within the encoder layers. The outputs from the last encoder block serve as input features for the pooling layer.
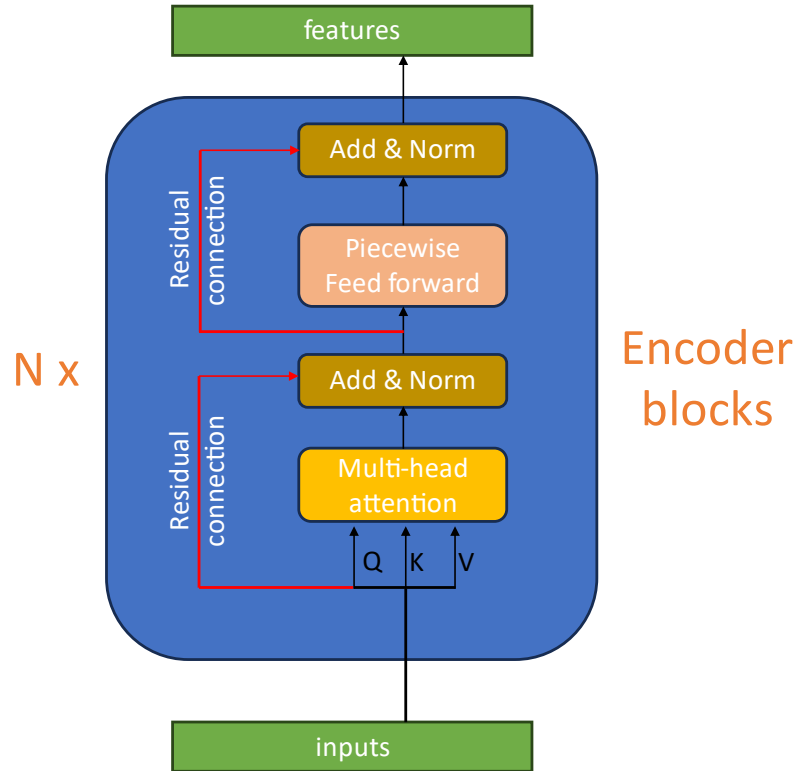
Figure 5.3: Encoder layer details

5.3 Experiment Setup and Data Collection

5.3.1 Experiment Setup

For precisely measuring position with certain trajectories and the corresponding tissue reaction force, biopsy system (shown in Figure 5.4) with 6 degree of freedom (DOF) consists a potentiometric position sensor (IR robot: IR-10kΩ linearity potentiometer), a force measurement sensor (ATI model: Nano 43 Transducer), a biopsy cut needle (Bard instrument: 16-gauge/1.7mm). Robotic needle biopsy system is well developed under force/position control loop and can achieve 0.04mm precision. These components work in tandem to replicate the conditions encountered during actual medical procedures, enabling a comprehensive assessment of the system performance in a controlled laboratory environment.
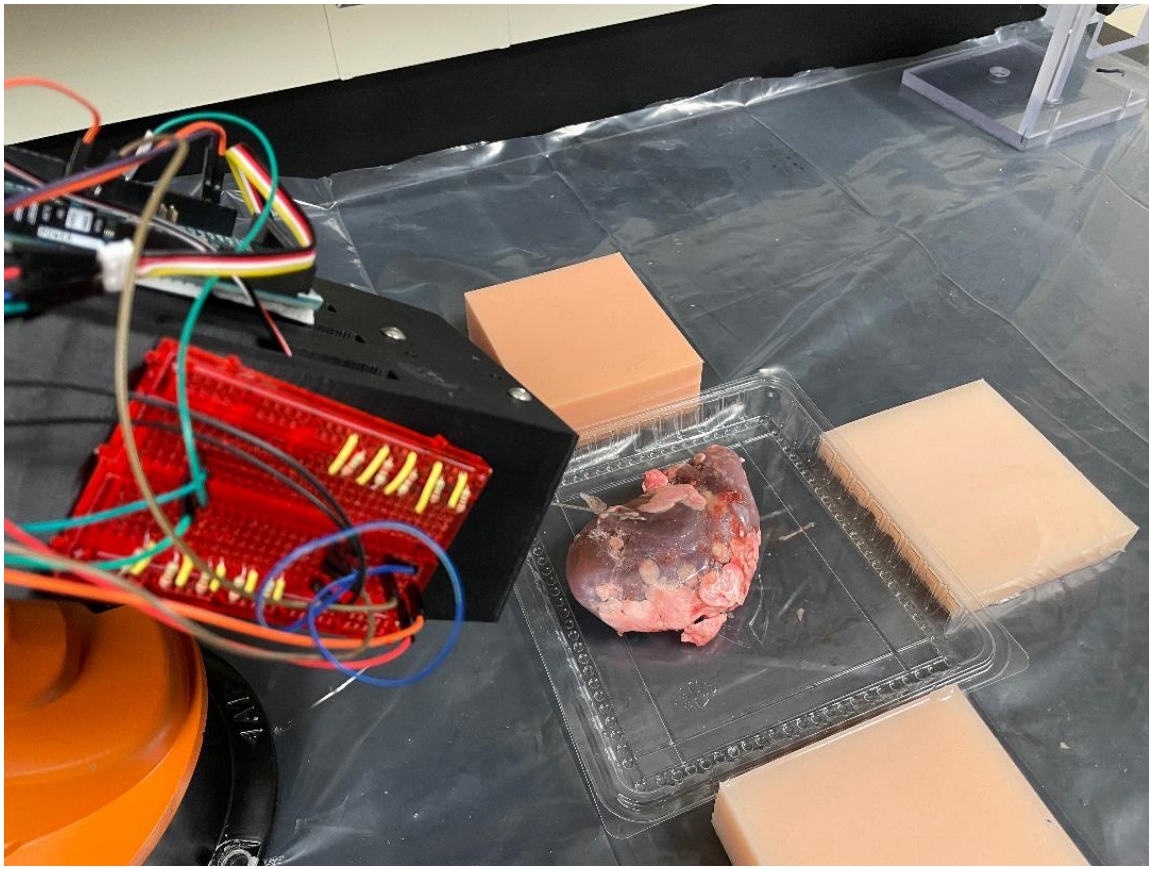
Figure 5.4: Biopsy system setup for kidney tissue interaction data collection

5.3.2 Data Collection

The experimental setup for the robotic needle biopsy system involved the use of five distinct types of porcine tissues, including the liver, kidney, heart, belly, and hock tissues. These tissues were carefully harvested to provide a diverse range of samples for testing and analysis. To ensure stability and precision during the experiments, a prototype of the robotic needle biopsy system was securely positioned on an experiment table. Additionally, a specially designed holder was employed to firmly secure the porcine tissue samples, ensuring consistent positioning and minimizing variability in the experimental conditions.

To standardize the experimental process, the porcine tissue samples were sectioned to approximately 30mm in thickness, ensuring uniformity across all samples. The robotic needle biopsy system then conducted a series of 50 distinct needle insertion procedures for

each tissue section. These procedures were carried out with a constant feeding speed of 2mm/s, maintaining consistency in the needle insertion process. During each of these procedures, the system recorded each data frame for each procedure, including the corresponding reaction force exerted on the needle, the displacement of the needle within the tissue, and the data points of 20 Hz. Needle puncture timestamp is also recorded for labeling.

The data gathered from these experiments offer valuable insights into the mechanical properties and different phases of various porcine tissues during needle biopsy procedures. A typical recorded displacement-force sample data profile, depicted in Figure 5.1(a), visually portrays the correlation between the displacement of the needle and the corresponding reaction force. This representation is crucial for understanding the mechanics of the tissue and the forces involved during the biopsy process.

5.3.3 Data Labeling

The primary objective of the transformer classification model is to accurately detect transitions during needle-puncture events and classify the various tissue types involved. To train the transformer classification model, data collection was conducted during the experimental setup. Timestamps were carefully recorded to capture when critical events as the tissue punctures occurred. During the data collection process, we carefully measured timestamps when these critical events occurred within the experimental setup. By applying the time-displacement profile, we can locate the critical puncture event precisely with respect to the needle travel displacement.
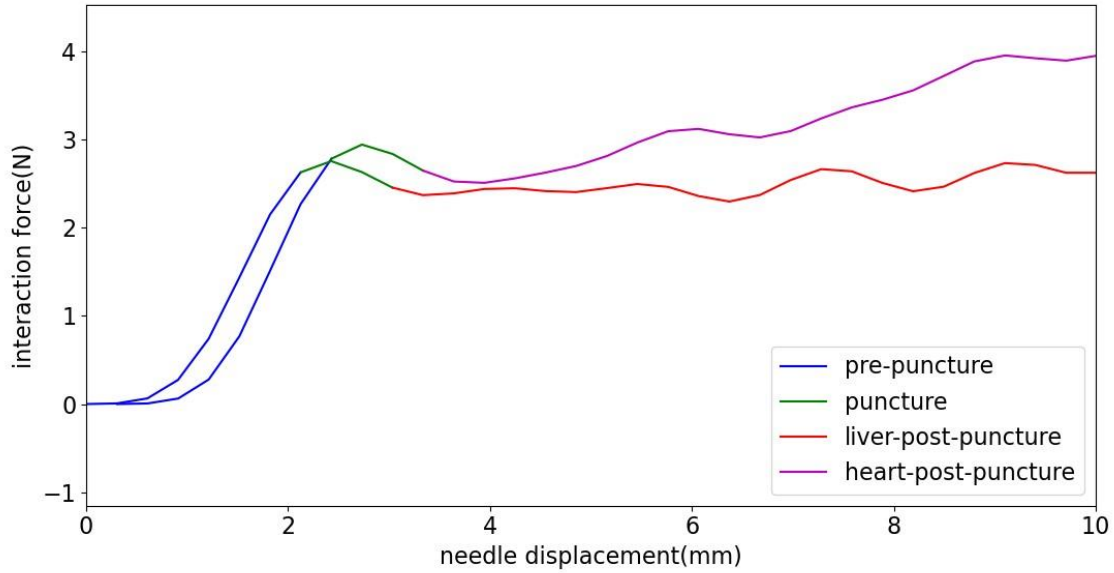
Figure 5.5: Data labeling example of events and types for liver and heart tissues

An example of mixture labeling of events and tissue types is shown in Figure 5.5. During the initial phase of needle feeding, as indicated by the blue curves in Figure 5.5, the tissue surface has not yet been penetrated. In this pre-puncture phase, it is inherently challenging to pinpoint the specific tissue type accurately. This is due to the lack of direct contact and interaction between the needle and the tissue surface. As the needle continues to feed into the tissue, a significant and identifiable event occurs—puncture. This is characterized by a notable drop in the interaction force, as illustrated by the green curves in Figure 5.5. This phase is marked by the actual penetration of the needle into the tissue. Following the puncture phase, the needle interacts differently with the tissue. Friction and cutting forces become dominant, leading to distinct force dynamics. During this post-puncture phase, the data becomes more suitable for tissue type classification, as indicated by the red and purple curves in Figure 5.5. These labels correspond to specific tissue types encountered during the post-puncture phase, facilitating accurate classification based on the unique force profiles exhibited by each tissue type.

Thus, we create the following label types to meet the main aim of detecting the transition in needle-puncture events and classify the different tissue types:

①. all tissues have a free-load/stop phase.

②. all tissues have a pre-puncture phase.

③. all tissues have a puncture phase.

④. different labels (Ⓛ for liver, Ⓚ for kidney, Ⓗ for heart, Ⓑ for belly, and Ⓒ for hock tissues) will be assigned for each post-puncture phase.

For example, a typical heart tissue would have a sequence of labels with respect to time as ①→①→①→②→②→③→③→ Ⓗ → Ⓗ → Ⓗ → Ⓗ →① during its needle insertion process. To notice, this label sequence does not strictly match the period. The example sequence is just a demonstration of label-changing behavior in a heart needle insertion process.

5.3.4 Low Pass Filtering and Data Augmentation

Following the collection and labeling of data from the force and position channels, a crucial step in the data processing pipeline involves applying a 6th-order Butterworth low pass filter. This filtering operation is essential for refining and conditioning the data, enhancing its quality and usability for subsequent analysis. In this specific implementation, the sampling rate for the force and position signals is set at 20Hz. The cutoff frequency for the Butterworth low pass filter is determined to be 10Hz. The cutoff frequency marks the point at which the filter begins to reduce the amplitude of high-frequency noises while the low-frequency interaction information is maintained.

For each kind of tissue, eight harvested sections are tested. There are overall 8(sections)*50(procedures)*5(types) = 2000 raw data frames. The amount of training data required for effective training can vary depending on the complexity of the task, the specific architecture used, and the characteristics of the dataset. However, as a general

observation, Transformers often require more training data compared to other deep learning architectures. We develop the following data augmentation algorithm to enrich the dataset.

In our raw datasets, each data frame comprises 120 timestamps, 120 position records, 120 force records, and 120 corresponding labels. Each timestamp is synchronized with its respective position, force, and label records. You can see the raw data frame structure in Figure 5.6(a). To enhance our dataset, we applied a zero-padding enrichment technique, illustrated in Figure 5.6(b). Here, we added 60 timestamps and data points to the beginning of the raw data frame, with sequential timestamps, while setting both position and force to zero. The labels for these 60 timestamps were uniformly assigned as Ⅰ (free-load/stop phase). Following this enrichment, we randomly selected 40 samples from the dataset, ensuring that their starting points were within the zero-padded region. However, the length of each sample remained at 120 timestamps. The label for each of these samples was designated as the last label in the new windowed data frame, as demonstrated in Figure 5.6(c).
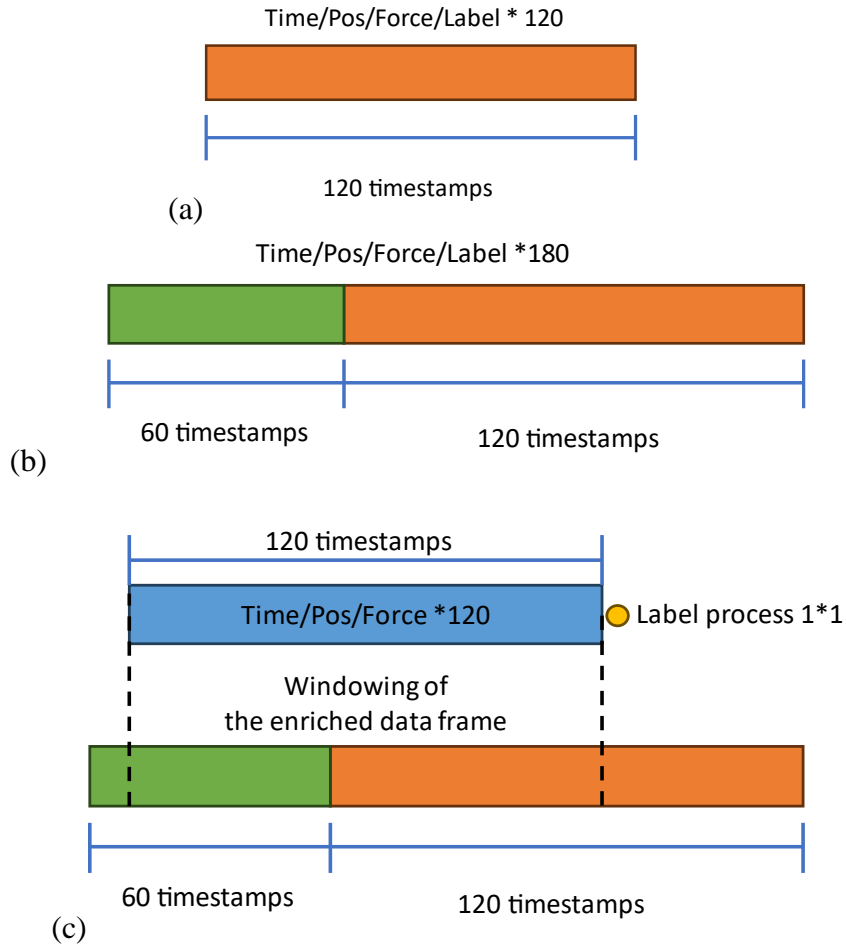
Figure 5.6: Data augmentation. (a) Raw data frame. (b) Extended data frame. (c) Random windowing selection from extended data frame.

As our aim is to build a state classifier for time series data, we care about the label corresponding to the last timestamp the most. Therefore, we reduce the label from 120*1 into 1*1. By this data augmentation algorithm, we enrich the overall dataset from 2000 raw data frames into 80,000 data frames. This enriched dataset provides adequate examples for the transformer classification method to learn from, allowing the model to capture various patterns and states within the time series data effectively. The increased dataset size contributes to the model's accuracy and generalizability, enhancing its ability to classify different states or conditions accurately. Moreover, the decision to employ a single conclusive label for the last timestamp greatly enhances the efficiency of the transformer

model's training and classification processes. With a simplified label format, the model can straightly process and learn from the data, leading to enhanced classification effectiveness.

5.4 Model Training and Evaluation Metrics

For a comprehensive classifier for the overall objectives, we need to have a transformer model trained based on various tissue datasets. Our input data is represented as $X \in R^{B \times T \times F}$ and corresponding label $Y \in R^B$ in a batch, where B stands for batch size, T stands for timestamps in one data frame, and F stands for features input to the model, which in our case F is 2 channels containing force and needle displacement. A linear projection and embedding layer are implemented to explicitly to retain the information regarding the order of signals in the time sequence. The output from the embedding layer would be $E \in R^{B \times 2T}$. Next, we construct an encoder layer, and the output E is fed into the multi-head attention module within one of the N encoder blocks to extract valuable information. The multi-head attention module consists of M heads, and each head processes the input independently.

For the M-th head, we construct query Q_m, key K_m and value V_m from input E, attention [60] can be calculated as the following:

$$Attetion = H_m(Q_m, K_m, V_m) = softmax\left(\frac{Q_m K_m^T}{\sqrt{d_k}}\right) V_m$$

where K_m^T is the transpose of K_m, $\frac{1}{\sqrt{d_k}}$ is the scaling factor and d_k is the dimension of Q_m, K_m, V_m. By concatenating the output of M heads together, we can obtain the aggregated temporal feature H for each data frame. To preserve the original features and prevent excessive smoothing during the classification process, we combine E and H then pass them through a layer-normalization layer, resulting in L. L is then processed by a feed forward layer and then by a layer-normalization layer to obtain the output O of one of the

N encoder blocks. In our model, we set number of heads as 8 and head size as 256. Four encoder blocks are contained in the encoder layer.

The transformer classification model is implemented with Keras on Tensorflow [61]. 80% of the dataset is set for training and testing, 20% of the dataset is set for evaluation. The evaluation of the tissue recognition algorithm typically relies on the accuracy metric. However, it is generally not possible to identify the tissue type before the puncture takes place [62]. In practical applications, our primary focus is on the different stages of needle insertion process. Thus, we introduce 3 measures: accuracy for classifying pre-puncture phase as A_{pre}, accuracy for classifying puncture phase as A_{punc}, accuracy for classifying tissue types in post-puncture phase as A_{tissue}. The objective of the three metrics is to assess the classifier's performance on the different stages of the needle insertion. Under A_{tissue}, distinct tissue classification precision is also recorded as A_L, A_k, A_H, A_B, A_C for liver, kidney, heart, belly, and hock. The general computation formula for accuracy is stated as following:

$$Accuracy = \frac{correct\ predictions}{total\ predictions} = \frac{TN + TP}{TN + TP + FN + FP}$$

Total predictions are the number of data frames in the evaluation dataset. TP is the number of true positive predictions, for examples, are puncture classes that are classified as puncture. TN is the number of true negative predictions, for examples, when we are computing A_{punc}, are all other classes which are not classified as puncture [63].

In order to rigorously evaluate the proposed method's effectiveness and its potential advantages, a series of comparative experiments are conducted. The aim of these experiments was to contrast the proposed approach with two well-established temporal classification modeling techniques, namely the RNN-LSTM model and the CNN model. This head-to-head comparison serves to elucidate the strengths and capabilities of the new method in the context of tissue classification tasks. RNN-LSTM is renowned for its ability

to capture sequential dependencies in data. Researchers have developed recurrent networks to aid the haptic feedback [64] or to classify tissue [5]. While CNN excels in extracting spatial-temporal features, former researchers also conducted experiments to investigate influence of dimensionality reduction on force estimation in robotic-assisted surgery [65]. For RNN-LSTM, we here applied 2 LSTM layer with a normalization of 256 nodes, and finalized with a softmax classification layer. For CNN, 3 CNN layers with 64, 128 and 256 filters connect to dense layer with 2048, 1024 and 512 with RELU activation, and finalized with a softmax classification layer.

All training, testing and offline validation is conducted on 8 RTX 2080TI GPU and Intel(R) Xeon(R) CPU E5-2697A v4 @ 2.60GHz.

5.5 Result and Evaluation on Classification

In the following section, we provided qualitative and quantitative results from our experiments with offline classification accuracy evaluation and online classification result.

5.5.1 Offline classification accuracy evaluation

The accuracy of the proposed classification algorithm is measured on an independent validation set, and the results for different models using metrics A_{pre}, A_{punc}, and A_{tissue} are gathered in Table 5.1.

Method	Metric type	Acc [%]
Transformer	A_{pre}	95.10%
	A_{punc}	94.58%
	A_{tissue}	91.20%
RNN-LSTM	A_{pre}	92.27%
	A_{punc}	90.11%
	A_{tissue}	85.84%
CNN	A_{pre}	87.77%
	A_{punc}	88.34%
	A_{tissue}	81.56%

Table 5.1: Accuracy comparison measured on validation set.

Based on the data presented in Table 5.1, it is evident that the Transformer model consistently outperforms the other models across all metrics. During the pre-puncture phase, the Transformer model achieves an impressive accuracy of 95.3%, and for puncture phase and post-puncture phase, transformer achieved 94.2% and 91.7%, respectively. RNN-LSTM is the runner-up, it delivers reliable results with an accuracy of 92.27% during the pre-puncture phase. However, its performance in the puncture and post-puncture phases is not as impressive, achieving accuracies of 90.11% and 85.84%, respectively. CNN model performs the least effectively among the three models, yielding accuracy scores of 87.77% in the pre-puncture phase, 88.34% in the puncture phase, and 81.56% in the post-puncture phase.

The detailed accuracy confusion matrix for transformer can be referred to the confusion matrix in Figure 5.7. From the confusion matrix, it is worth noting that in some instances, the heart tissue is classified as hock. This observation can be attributed to the similarity in muscle composition and resulting mechanical properties between the heart and hock tissues. Such occasional classification overlap is generally acceptable due to these similarities, and it underscores the importance of refining the classification model to achieve even more precise differentiation in such scenarios.
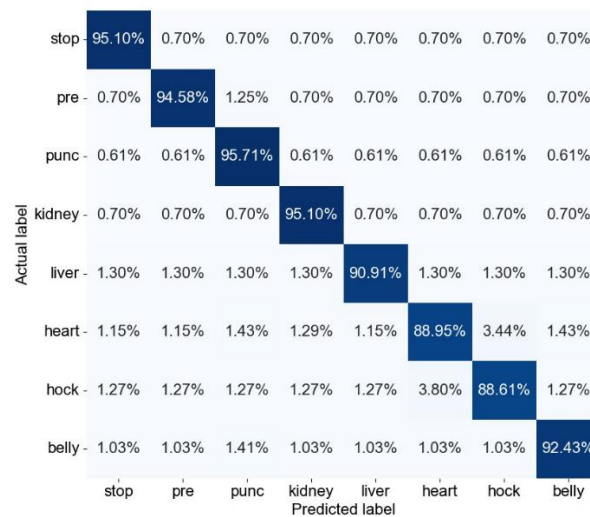

Figure 5.7: Confusion matrix for Transformer classification model.

5.5.2 Online classification

In our study, we developed an online classification system in which a needle was employed for biopsy procedures on liver tissue and heart tissue. The tissue types are intentionally kept unknown during the experiment. The needle is used to probe the tissue, and real-time data, including time, force, and needle displacement, are collected to form our input dataset. To facilitate real-time predictions, we integrate the most effective model, which is a transformer model, based on our training results, into the experimental setup. To supply data to the model, a data frame consisting of 120 data points from the sensors is created and provided as input. In cases where the data frame contains fewer than 120 data points, we apply the same zero-padding technique introduced in Section 2.3.3 to ensure that the data frame reaches the desired length. We gathered data and ran all processing on CPU (Intel i9-13900H @ 2.600GHz) and GPU (NVIDIA GeForce GTX 4060) for the online tissue classification. In the case of the transformer model, the resulting inference time is below the targeted threshold of 10 ms, while the sampling rate of data collection is 20Hz (50ms).

In Figure 5.8, you can observe that for each tissue type, the force/displacement profile is depicted in blue, alongside the label generated from online classification with respect to displacement is marked by red lines, the actual label is marked by green lines. The needle started from air for all tissue types, reaching the tissue surface with a constant speed of 2mm/s. Needle then fed in the region of interest, punctured into the surface with the same speed. From Figure 5.8, it is seen that for every tissue type, the pre-puncture and puncture phases were well detected. Very few error labels are generated during these periods. As the needle enters the post-puncture phase, distinct tissue labels are generated, and the overall classification accuracy is found to be satisfactory.
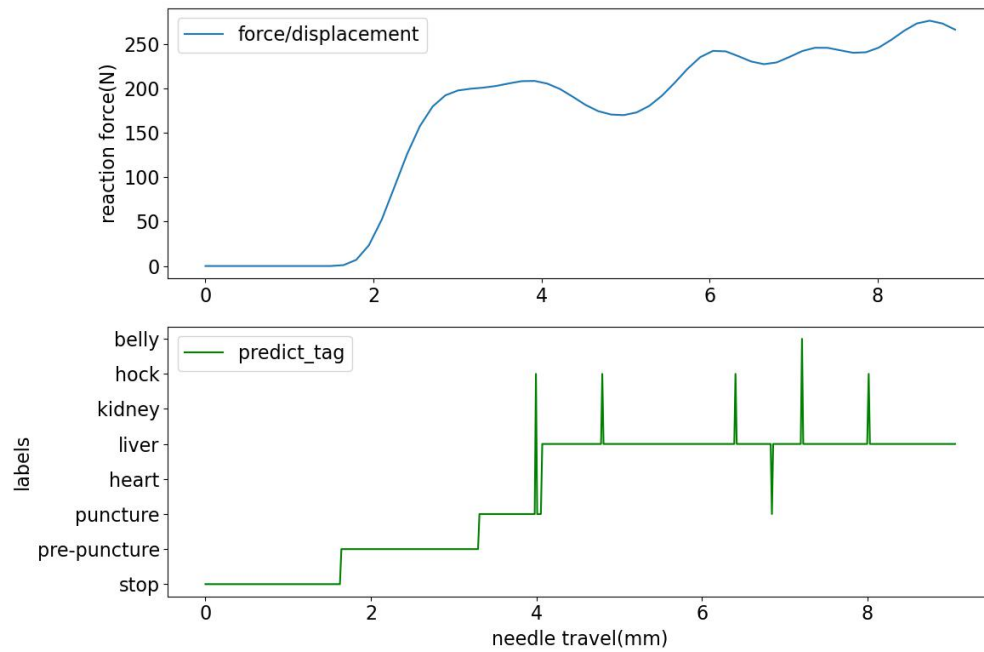
(a)
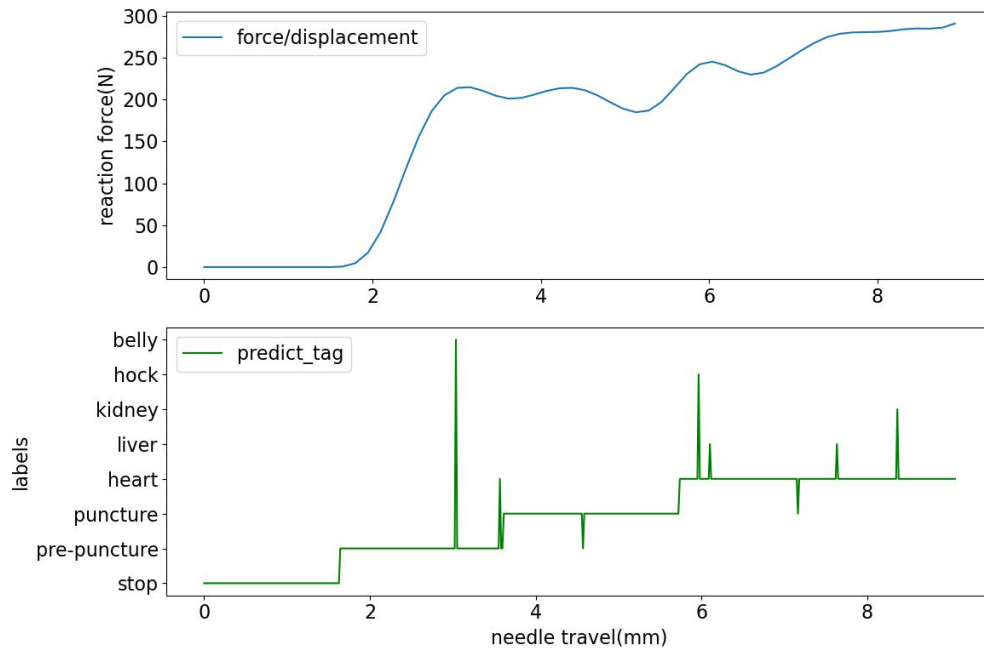
(b)

Figure 5.8: Online classification result with needle force/displacement profile. (a) classification result with heart. (b) classification result with liver.

5.6 Model Expansion on Force Prediction

Moreover, we would like to expand our application into force prediction for surgeons' reference while the insertion process is carried out. This would lead into a different stage where surgeons could be guided and informed by the reference force/displacement profile for environment understanding. As surgery type is ensured and region of interest is pre-recorded under MRI or ultrasonic imaging, puncture event can be predicted from the needle-surface distance using a pre-trained model. Once the needle is inserted into the tissue, the system can generate real-time force/displacement profiles. This process combines pre-trained data with observed force data, enabling the system to provide immediate feedback on the forces experienced by the needle. As the needle progresses in tissue towards the target focal area with potentially abnormal tissue properties, the force prediction aims to generate profiles that resemble the short-term force dynamics that the needle will encounter in the near future. This ensures that the surgeon remains informed and prepared for the evolving conditions within the tissue. One of the critical functionalities of force prediction is to detect any notable changes in the force/displacement profiles. If the profile deviates significantly from the expected pattern, the system can promptly inform the surgeon of this change. This serves as a valuable alert mechanism, enabling the surgeon to recognize when the needle is approaching a focal area with unique tissue properties. Such timely information empowers the surgeon to adjust their approach, enhancing the precision and safety of the surgical procedure.

As referred to the Figure 5.1, the processing model of the transformer remains the same, while for the output modules as the prediction module, another pooling layer and feed-forward layer within the prediction layer [66] are utilized to forecast force parameters over sequential short periods, with the assumption that needle feeding speed would remain the same. Both RNN-LSTM and CNN model mentioned in section 5.2 are also trained and tested on the force prediction module.

In force prediction, a different evaluation metric should be applied to measure the performance of our model. It is typical to use the metric of root mean square error ($RMSE$) for quantitively analysis the predicted result with recorded real reaction force with certain periods [67]. The is defined as following:

$$RMSE = \sqrt{\frac{\sum_{t=1}^{N_s}\left[F(t) - \hat{F}(t)\right]^2}{N_s}}$$

where $\hat{F}(t)$ is the predicted force on timestamp t, $F(t)$ is the measured force on timestamp t, N_s is the sample points number that regulate the output format. The sampling rate keeps the same as 20Hz as mentioned in section 5.3.

Here is the Table 5.2 for $RMSE$ evaluation with different N_s sets on different tissues with different models.

Method	Tissue type	RMSE(Ns=20)	RMSE(Ns=40)	RMSE(Ns=60)
Transformer	liver	0.59	0.80	1.16
	heart	0.58	0.85	1.22
	kidney	0.66	0.85	1.18
	belly	0.52	0.76	1.16
	hock	0.65	0.67	1.12
RNN-LSTM	liver	0.76	1.05	1.49
	heart	0.81	1.02	1.56
	kidney	0.75	0.91	1.47
	belly	0.73	0.88	1.46
	hock	0.83	1.00	1.50
CNN	liver	1.02	1.42	2.02
	heart	1.09	1.71	2.27
	kidney	0.95	1.49	2.41
	belly	0.91	1.32	2.11
	hock	1.03	1.57	2.19

Table 5.2: RMSE comparison measured on different tissues with three models.

Analyzing the results presented in Table 5.2, it is evident that the Transformer model consistently outperforms other models. For a prediction time of 20 N_s (equivalent to 1 second), the Transformer model achieves an average $RMSE$ of 0.60. In contrast, the RNN-LSTM model and CNN yield $RMSE$ values of 0.78 and 1.00, respectively, for the same 20 N_s experiments. As the prediction time increases (indicated by larger N_s values), the prediction results tend to deviate more from the observed data points. Even in these scenarios, the Transformer model maintains its superiority. Specifically, for prediction times of 40 N_s and 60 N_s, the Transformer model produces $RMSE$ values averaging 0.79 and 1.17, respectively. In comparison, the RNN-LSTM model achieves higher $RMSE$ values of 0.97 and 1.50 on average for the 40 N_s and 60 N_s tests, while the CNN model predicts even worse, with $RMSE$ values averaging 1.50 and 2.20 for the 40 N_s and 60 N_s experiments. Moreover, it's noteworthy that the belly group consistently demonstrates the best performance among all the tissues. This is likely attributed to the higher fat composition in the belly tissue, making it relatively easier for the models to predict accurately.

5.7 Conclusion and Future AI Integration on Robotic Biopsy

This chapter introduces a groundbreaking approach that leverages the Transformer architecture to extract contextual information from time sequences of needle displacement and reaction forces, enhancing tissue classification. The key innovations and contributions are outlined as follows: (1) We present an advanced deep learning method based on the Transformer architecture, which proves highly effective in achieving tissue recognition. (2) Our approach involves detailed tissue modeling and categorizing the needle insertion process into three distinct phases. This scientific approach ensures the accuracy and rationality of tissue classification. (3) We perform real-time tissue classification on actual tissue samples, showcasing the practical applicability of our algorithm in real surgical

scenarios. (4) We expand our model into regression for tissue reaction force prediction, allowing us to identify when the needle approaches a focal area with unique tissue properties. In direct comparison with conventional temporal modeling-based frameworks, our proposed Transformer method consistently outperforms in tissue classification. This study offers a promising approach for robust and precise tissue classification, with broad applications in haptic biopsy sensing, ultimately enhancing the safety and effectiveness of medical procedures.

CHAPTER 6

CONCLUSION AND FUTURE WORK

6.1 Conclusion and Discussion

In this dissertation, an accurate computer-aided digital needle biopsy system has been presented. To facilitate the incorporation of intelligence and advanced diagnostic approach into medical robotic systems, a comprehensive system architecture is imperative, capable of accommodating artificial intelligence, safety control, trajectory planning, and swift diagnosis. The primary goal of such intelligent architectures is to seamlessly merge system control with trajectory planning and artificial intelligence, harnessing data from various sources. The generalized subsystem encompasses a trajectory planner, a semi-autonomous safety controller, a robotic platform with a robotic manipulator and insertion module, a tissue classification unit, and a digital pathology unit. This intelligent system architecture, complete with these subsystems, is illustrated in Figure 6.1.
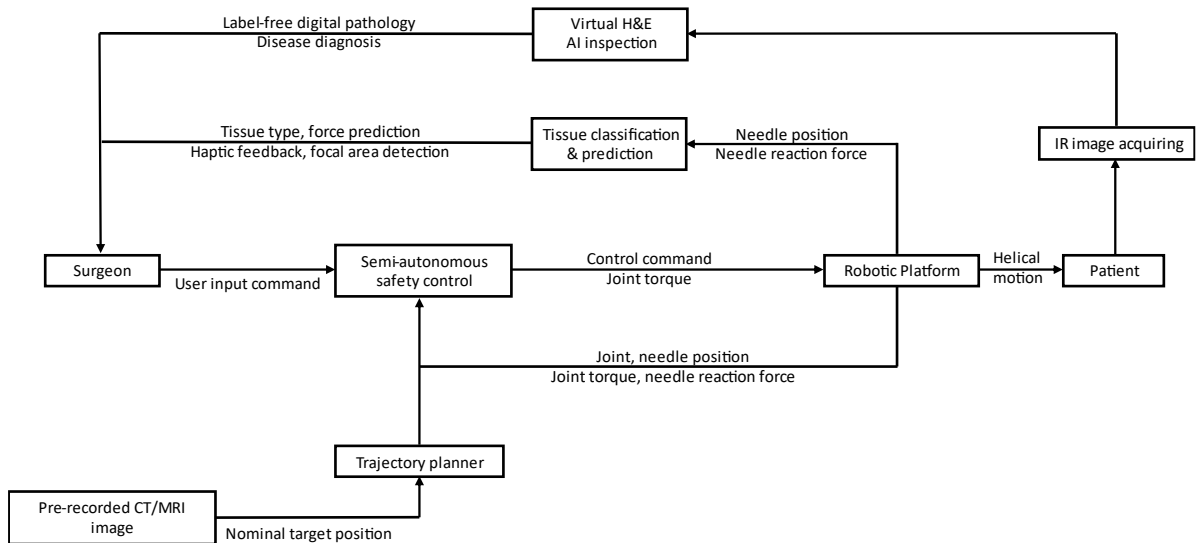
Figure 6.1: Intelligent System for Biopsy Robotic System

- Design and Development of Fiber-optic Compatible Robotic Biopsy System

This innovative robotic biopsy system is characterized by its high dexterity, comprehensive workspace modeling, and an in-depth understanding of system dynamics. To achieve precise access to the target location, it is crucial to identify the needle penetration trajectory that brings the needle closest to the focal area while avoiding vasculatures or organs in its path. An automatically optimized trajectory planner can be customized based on pre-recorded CT/MRI images and any region-specific constraints. Changes in the surgical environment or the procedure are continuously monitored by tracking sensor devices, and recommendations for trajectory adjustments can be made through surgeon intervention. These features collectively unlock the full potential of the biopsy system, offering increased precision and versatility.

Moreover, I have showcased compatibility with label-free digital pathology. To expedite the diagnostic process, we have ensured fiber-optic tool compatibility through a spring-loaded roller mechanism. A specialized helical motion can be employed with the insertion module to guarantee the acquisition of sufficient molecular information in an in-situ environment. The molecular image reconstruction scheme is also delineated, accompanied by an example of image reconstruction based on stacked reflectance points. This analysis has thoroughly unveiled the potential of employing label-free digital pathology for in-situ molecular analysis and disease diagnostics.

- Development of a Semi-Autonomous Safety Control

In addition, the creation of a semi-autonomous safety control system for the robotic platform ensures that robotic movements are both precise and safe, addressing critical safety concerns associated with these advanced medical technologies. This development contributes to the overall effectiveness and reliability of the robotic biopsy system. The control algorithms are tested and validated, ensuring the precision of robotic movement with safety concerns.

- Development of a Novel Intelligent System for Robotic Biopsy

To ensure the precise location of the focal area, tissue classification and prediction play a pivotal role. Data from needle interaction forces and displacements collected through sensor inputs are fed into the classification and prediction model. The transformer model's inference generates tissue information and a sequential prediction of force profiles. This haptic force feedback, along with tissue type information and sequential force predictions, is provided to the surgeon to enhance environmental sensing. In cases where tissue properties undergo significant changes, the system alerts the surgeon to facilitate the detection of focal areas. The transformer-based classification algorithm embodies a remarkable advancement in robotic biopsy assistance, featuring the development of an intelligent system that integrates detailed mechanics modeling of needle-tissue interactions with a deep-learning model based on needle insertion forces. This model not only enhances our understanding of these interactions but also excels in tissue classification, outperforming current methodologies. Moreover, it extends its capabilities into force prediction, augmenting surgeon precision during needle insertions. This multifaceted approach represents the vanguard of artificial intelligence in robotic biopsy assistance, promising to revolutionize biopsy procedures and significantly contribute to the next generation of medical technology.

The convergence of the robotic biopsy system, label-free digital pathology compatibility and the machine learning-based classification methodology presents the potential to transform the needle biopsy field. This synergy offers precise and accurate needle placement, access to detailed tissue composition, and real-time environment recognition. This foundational work sets the stage for the development of a highly accurate computer-aided digital needle biopsy system, promising to significantly enhance the efficacy and precision of biopsy procedures.

6.2 Future Directions of Research

6.2.1 Haptic Guidance in Needle Insertion

The primary classification method introduced in this context reveals the nature of the underlying tissue interacting with the biopsy tool. While this classification already provides a wealth of information surpassing what is available through visual feedback on commercially available surgical robotic platforms, there is an exciting opportunity to take this a step further by predicting haptic force feedback and generating haptic guidance prior to the actual insertion.

Haptic guidance can manifest in two key directions. Firstly, by utilizing pre-recorded MRI, CT, or ultrasound images, a 3D reconstruction of a specific region of interest and its surroundings can be created, resembling electroanatomic reconstruction [68-69]. The force/displacement profile image can be generated using the transformer method before a particular insertion direction is indicated. This offers a faster analysis of tissue deformation and resistance during needle insertion since it doesn't require the needle-displacement data to be fed into the model for an adaption.

On the other hand, haptic guidance can be employed to detect abnormal tissue and assist in localizing the region of interest [70]. For instance, a stable, predictable needle insertion can be indicated by the force/displacement profile, but when encountering abnormal or focal tissue, the change in mechanical properties can be detected by the force prediction transformer model [71]. This alerts the surgeons to be prepared for either digital pathology operations or tissue retraction, with the potential to significantly enhance the efficacy and precision of biopsy procedures. This innovative approach holds great promise for improving patient outcomes and the overall biopsy process.

6.2.2 Utilizing Digital Pathology for In-situ Biopsy Surgery

This dissertation has presented the compatibility of integrating label-free digital pathology and the potential advantages of reducing operation time while increasing efficiency. By applying automated molecular information classification algorithms, Quantum Cascade Laser (QCL) based detection can achieve a sensitivity of 96% and a specificity of 100%, comparable to the slower Fourier-transform infrared (FTIR) imaging [72].

However, to take the next step in real QCL-based applications, several adaptations are required. Firstly, the development of specialized fiber-optic tools is essential. Traditional optic-fiber connections would involve a capsule-based connection hinge between the optic-fiber and the laser output component. Given the need for helical motion at the end-tip of the tool, the optic-fiber would rotate with the motor drive, while the QCL and lens base remain stationary. This rotation could lead to fiber twisting, potentially damaging the fiber itself. Thus, a unique capsule mounting for the fiber, QCL, and lens base is necessary [73]. An emerging trend is the development of Fiber-Optic Needles capable of directly transmitting spectroscopic information, as demonstrated by researchers developing Interstitial Fiber-Optic Needles for Cancer Sensing and Therapy [74].

Secondly, inverse display and computation for helical raw data must be implemented, as well as the development of a molecular information retraction algorithm. With the tool performing a helical motion, a set of pixels are recorded (illustrated as in Chapter 3.3). Thus, inverse display and computation are necessary for data processing. Additionally, given that molecular information is recorded in this specific pattern, an information retraction algorithm should be developed to meet this need, facilitating the interpretation and utilization of the data. These adaptations are crucial for advancing the capabilities of QCL-based applications and ensuring the accurate retrieval of molecular information.

REFERENCES

[1] O. Kiamanesh and M. Toma, "The State of the Heart Biopsy: A Clinical Review," CJC Open, vol. 3, no. 4, pp. 524–531, Apr. 2021, doi: https://doi.org/10.1016/j.cjco.2020.11.017.

[2] A. L. McKnight, J. L. Kugel, P. J. Rossman, A. Manduca, L. C. Hartmann, and R. L. Ehman, "MR Elastography of Breast Cancer: Preliminary Results," American Journal of Roentgenology, vol. 178, no. 6, pp. 1411–1417, Jun. 2002, doi: https://doi.org/10.2214/ajr.178.6.1781411.

[3] Inko Elgezua, S. Song, Y. Kobayashi, and M. G. Fujie, "Online Event Classification for Liver Needle Insertion Based on Force Patterns," Springer eBooks, pp. 1145–1157, Sep. 2015, doi: https://doi.org/10.1007/978-3-319-08338-4_83.

[4] T. Lehmann, C. Rossa, N. Usmani, R. S. Sloboda, and M. Tavakoli, "Intraoperative Tissue Young's Modulus Identification During Needle Insertion Using a Laterally Actuated Needle," IEEE Transactions on Instrumentation and Measurement, vol. 67, no. 2, pp. 371–381, Feb. 2018, doi: https://doi.org/10.1109/tim.2017.2774182.

[5] N. Sankaran and Thenkurussi Kesavadas, "RNN-LSTM based Tissue Classification in Robotic System for Breast Biopsy," Nov. 2020, doi: https://doi.org/10.1109/biorob49111.2020.9224378.

[6] F. J. Siepel, B. Maris, M. K. Welleweerd, V. Groenhuis, P. Fiorini, and S. Stramigioli, "Needle and Biopsy Robots: a Review," Current Robotics Reports, vol. 2, no. 1, pp. 73–84, Jan. 2021, doi: https://doi.org/10.1007/s43154-020-00042-1.

[7] M. D'Souza, J. Gendreau, A. Feng, L. H. Kim, A. L. Ho, and A. Veeravagu, "Robotic-Assisted Spine Surgery: History, Efficacy, Cost, And Future Trends," Robotic Surgery: Research and Reviews, vol. Volume 6, pp. 9–23, Nov. 2019, doi: https://doi.org/10.2147/rsrr.s190720.

[8] S. Amack et al., "Design and control of a compact modular robot for transbronchial lung biopsy," PubMed Central, Mar. 2019, doi: https://doi.org/10.1117/12.2513967.

[9] M. Muntener et al., "Magnetic resonance imaging compatible robotic system for fully automated brachytherapy seed placement," Urology, vol. 68, no. 6, pp. 1313–1317, Dec. 2006, doi: https://doi.org/10.1016/j.urology.2006.08.1089.

[10] G. Minchev et al., "A novel miniature robotic guidance device for stereotactic neurosurgical interventions: preliminary experience with the iSYS1 robot," Journal of Neurosurgery, vol. 126, no. 3, pp. 985–996, Mar. 2017, doi: https://doi.org/10.3171/2016.1.jns152005.

[11] R. P. Felten, N. Ogden, C. Peña, M. C. Provost, M. J. Schlosser, and C. Witten, "The Food and Drug Administration Medical Device Review Process," Stroke, vol. 36, no. 2, pp. 404–406, Feb. 2005, doi: https://doi.org/10.1161/01.str.0000153063.54972.91.

[12] E. Franco, Djordje Brujić, M. Rea, Wladyslaw Gedroyc, and M. Ristić, "Needle-Guiding Robot for Laser Ablation of Liver Tumors Under MRI Guidance," IEEE-ASME

Transactions on Mechatronics, vol. 21, no. 2, pp. 931–944, Apr. 2016, doi: https://doi.org/10.1109/tmech.2015.2476556.

[13] Arvind Bhimaraj, B. Trachtenberg, and M. Valderrábano, "Robotically Guided Left Ventricular Biopsy to Diagnose Cardiac Sarcoidosis," Circulation-heart Failure, vol. 11, no. 3, Mar. 2018, doi: https://doi.org/10.1161/circheartfailure.117.004627.

[14] E. Ammirati et al., "State-of-the-Art of Endomyocardial Biopsy on Acute Myocarditis and Chronic Inflammatory Cardiomyopathy," Current Cardiology Reports, vol. 24, no. 5, pp. 597–609, Feb. 2022, doi: https://doi.org/10.1007/s11886-022-01680-x.

[15] P. Beard, "Biomedical photoacoustic imaging," Interface Focus, vol. 1, no. 4, pp. 602–631, Jun. 2011, doi: https://doi.org/10.1098/rsfs.2011.0028.

[16] Sandeep Saxena and T. A. Meredith, Optical coherence tomography. New York, Ny: Mcgraw-Hill Medical, 2008.

[17] B. G. Saar, C. W. Freudiger, J. Reichman, C. M. Stanley, G. R. Holtom, and X. S. Xie, "Video-Rate Molecular Imaging in Vivo with Stimulated Raman Scattering," Science, vol. 330, no. 6009, pp. 1368–1370, Dec. 2010, doi: https://doi.org/10.1126/science.1197236.

[18] C. R. Weiss, S. G. Nour, and J. S. Lewin, "MR-guided biopsy: A review of current techniques and applications," Journal of Magnetic Resonance Imaging, vol. 27, no. 2, pp. 311–325, 2008, doi: https://doi.org/10.1002/jmri.21270.

[19] W. J. Frable, "Fine-needle aspiration biopsy: a review," Human Pathology, vol. 14, no. 1, pp. 9–28, Jan. 1983, doi: https://doi.org/10.1016/s0046-8177(83)80042-2.

[20] M. Ahmed, Arnie Purushotham, and M. Douek, "Novel techniques for sentinel lymph node biopsy in breast cancer: a systematic review," Lancet Oncology, vol. 15, no. 8, pp. e351–e362, Jul. 2014, doi: https://doi.org/10.1016/s1470-2045(13)70590-4.

[21] H. H. Malluche, M. Chris Langub, and Marie‑Claude Monier‑Faugere, "The role of bone biopsy in clinical practice and research," Kidney International, vol. 56, pp. S20‑S25, Dec. 1999, doi: https://doi.org/10.1046/j.1523-1755.1999.07313.x.

[22] D. M. Elston, E. J. Stratman, and S. J. Miller, "Skin biopsy: Biopsy issues in specific diseases," Journal of the American Academy of Dermatology, vol. 74, no. 1, pp. 1–16, Jan. 2016, doi: https://doi.org/10.1016/j.jaad.2015.06.033.

[23] T. J. Grabowski, "Brain biopsy in dementia," Yearbook of Neurology and Neurosurgery, vol. 2007, pp. 102–103, Jan. 2007, doi: https://doi.org/10.1016/s0513-5117(08)70069-3.

[24] A. A. Renshaw and N. Pinnar, "Comparison of Thyroid Fine-Needle Aspiration and Core Needle Biopsy," American Journal of Clinical Pathology, vol. 128, no. 3, pp. 370–374, Sep. 2007, doi: https://doi.org/10.1309/07tl3v58337txhmc.

[25] R. J. Washabau et al., "Endoscopic, Biopsy, and Histopathologic Guidelines for the Evaluation of Gastrointestinal Inflammation in Companion Animals," Journal of

Veterinary Internal Medicine, vol. 24, no. 1, pp. 10–26, Jan. 2010, doi: https://doi.org/10.1111/j.1939-1676.2009.0443.x.

[26] E. B. Tapper and A. S.-F. . Lok, "Use of Liver Imaging and Biopsy in Clinical Practice," New England Journal of Medicine, vol. 377, no. 8, pp. 756–768, Aug. 2017, doi: https://doi.org/10.1056/nejmra1610570.

[27] R. Bhargava and A. Madabhushi, "Emerging Themes in Image Informatics and Molecular Analysis for Digital Pathology," Annual Review of Biomedical Engineering, vol. 18, no. 1, pp. 387–412, Jul. 2016, doi: https://doi.org/10.1146/annurev-bioeng-112415-114722.

[28] F. Großerueschkamp, H. Jütte, K. Gerwert, and A. Tannapfel, "Advances in Digital Pathology: From Artificial Intelligence to Label-Free Imaging," Visceral Medicine, pp. 1–9, Aug. 2021, doi: https://doi.org/10.1159/000518494.

[29] M. J. Baker et al., "Using Fourier transform IR spectroscopy to analyze biological materials," Nature Protocols, vol. 9, no. 8, pp. 1771–1791, Jul. 2014, doi: https://doi.org/10.1038/nprot.2014.110.

[30] B. R. Wood, L. Chiriboga, H. Yee, M. A. Quinn, D. McNaughton, and M. Diem, "Fourier transform infrared (FTIR) spectral mapping of the cervical transformation zone, and dysplastic squamous epithelium," Gynecologic Oncology, vol. 93, no. 1, pp. 59–68, Apr. 2004, doi: https://doi.org/10.1016/j.ygyno.2003.12.028.

[31] N. Amharref et al., "Brain tissue characterisation by infrared imaging in a rat glioma model," vol. 1758, no. 7, pp. 892–899, Jul. 2006, doi: https://doi.org/10.1016/j.bbamem.2006.05.003.

[32] S. Natarajan et al., "Clinical application of a 3D ultrasound-guided prostate biopsy system," Urologic Oncology: Seminars and Original Investigations, vol. 29, no. 3, pp. 334–342, May 2011, doi: https://doi.org/10.1016/j.urolonc.2011.02.014.

[33] S. C. Lee et al., "Contrast-Enhanced Ultrasound Imaging of Breast Masses: Adjunct Tool to Decrease the Number of False-Positive Biopsy Results," Journal of Ultrasound in Medicine, vol. 38, no. 9, pp. 2259–2273, Dec. 2018, doi: https://doi.org/10.1002/jum.14917.

[34] R. Heller et al., "In vivo gene electroinjection and expression in rat liver," FEBS Letters, vol. 389, no. 3, pp. 225–228, Jul. 1996, doi: https://doi.org/10.1016/0014-5793(96)00590-x.

[35] C. Basdogan, S. De Rensselaer, Jung Kim, M. Muniyandi, Hyun Kim, and M. A. Srinivasan, "Haptic rendering - beyond visual computing - Haptics in minimally invasive surgical simulation and training," IEEE Computer Graphics and Applications, vol. 24, no. 2, pp. 56–64, Mar. 2004, doi: https://doi.org/10.1109/mcg.2004.1274062.

[36] B. Ahn, H. Lee, Y. Kim, and J. Kim, "Robotic system with sweeping palpation and needle biopsy for prostate cancer diagnosis," The International Journal of Medical Robotics and Computer Assisted Surgery, vol. 10, no. 3, pp. 356–367, Oct. 2013, doi: https://doi.org/10.1002/rcs.1543.

[37] R. Heller et al., "In vivo gene electroinjection and expression in rat liver," FEBS Letters, vol. 389, no. 3, pp. 225–228, Jul. 1996, doi: https://doi.org/10.1016/0014-5793(96)00590-x.

[38] Severin Rodler et al., "A Systematic Review of New Imaging Technologies for Robotic Prostatectomy: From Molecular Imaging to Augmented Reality," Journal of Clinical Medicine, vol. 12, no. 16, pp. 5425–5425, Aug. 2023, doi: https://doi.org/10.3390/jcm12165425.

[39] N. K. Sankaran, P. Chembrammel, A. Siddiqui, K. Snyder, and T. Kesavadas, "Design and Development of Surgeon Augmented Endovascular Robotic System," IEEE Transactions on Biomedical Engineering, vol. 65, no. 11, pp. 2483–2493, Nov. 2018, doi: https://doi.org/10.1109/tbme.2018.2800639.

[40] C. Fang, Z. Wan, Y. Qiu, and C. Zhou, "A Compliance Control Strategy for Adapting to Body Movements during a Percutaneous Surgery," 2019 IEEE International Conference on Cybernetics and Intelligent Systems (CIS) and IEEE Conference on Robotics, Automation and Mechatronics (RAM), Nov. 2019, doi: https://doi.org/10.1109/cis-ram47153.2019.9095796.

[41] Giuseppe di Napoli, Alessandro Filippeschi, M. Tanzini, and Carlo Alberto Avizzano, "A novel control strategy for youBot arm," Oct. 2016, doi: https://doi.org/10.1109/iecon.2016.7793658.

[42] N. Egbers, C. Schwenke, A. Maxeiner, U. Teichgräber, and T. Franiel, "MRI-guided core needle biopsy of the prostate: acceptance and side effects," Diagnostic and

Interventional Radiology, vol. 21, no. 3, pp. 215–221, May 2015, doi: https://doi.org/10.5152/dir.2014.14372.

[43] K. Shyamala, H. Girish, and S. Murgod, "Risk of tumor cell seeding through biopsy and aspiration cytology," Journal of International Society of Preventive and Community Dentistry, vol. 4, no. 1, p. 5, 2014, doi: https://doi.org/10.4103/2231-0762.129446.

[44] R. J. Roesthuis, van Veen, A. Jahya, and S. Misra, "Mechanics of needle-tissue interaction," 2011 IEEE/RSJ International Conference on Intelligent Robots and Systems, Sep. 2011, doi: https://doi.org/10.1109/iros.2011.6094969.

[45] R. Barua, S. Datta, A. Roychowdhury, and P. Datta, "Study of the surgical needle and biological soft tissue interaction phenomenon during insertion process for medical application: A Survey," Proceedings Of The Institution Of Mechanical Engineers, Part H: Journal Of Engineering In Medicine, vol. 236, no. 10, pp. 1465–1477, Sep. 2022, doi: https://doi.org/10.1177/09544119221122024.

[45] A. M. Okamura, C. Simone, and M. D. O'Leary, "Force Modeling for Needle Insertion Into Soft Tissue," IEEE Transactions on Biomedical Engineering, vol. 51, no. 10, pp. 1707–1716, Oct. 2004, doi: https://doi.org/10.1109/tbme.2004.831542.

[46] M. Oldfield, D. Dini, G. Giordano, and Ferdinando, "Detailed finite element modelling of deep needle insertions into a soft tissue phantom using a cohesive approach," Computer Methods in Biomechanics and Biomedical Engineering, vol. 16, no. 5, pp. 530–543, May 2013, doi: https://doi.org/10.1080/10255842.2011.628448.

[47] L. Dong, S. Xu, and B. Xu, "Speech-Transformer: A No-Recurrence Sequence-to-Sequence Model for Speech Recognition," IEEE Xplore, Apr. 01, 2018. https://ieeexplore.ieee.org/document/8462506/

[48] Syed Waqas Zamir, A. Arora, S. Khan, M. Hayat, Fahad Shahbaz Khan, and M.-H. Yang, "Restormer: Efficient Transformer for High-Resolution Image Restoration," Jun. 2022, doi: https://doi.org/10.1109/cvpr52688.2022.00564.

[49] Y. Tay, D. Bahri, D. Metzler, D.-C. Juan, Z. Zhao, and C. Zheng, Synthesizer: Rethinking Self-Attention in Transformer Models. 2021. arXiv (Cornell University).

[50] S. Karita et al., "A Comparative Study on Transformer vs RNN in Speech Applications," 2019 IEEE Automatic Speech Recognition and Understanding Workshop (ASRU), Dec. 2019, doi: https://doi.org/10.1109/asru46091.2019.9003750.

[51] P. Han and K. Ehmann, "Study of the effect of cannula rotation on tissue cutting for needle biopsy," Medical Engineering & Physics, vol. 35, no. 11, pp. 1584–1590, Nov. 2013, doi: https://doi.org/10.1016/j.medengphy.2013.05.001.

[52] K. Jiang, P. Peng, Y. Lian, and W. Xu, "The encoding method of position embeddings in vision transformer," Journal of Visual Communication and Image Representation, vol. 89, p. 103664, Nov. 2022, doi: https://doi.org/10.1016/j.jvcir.2022.103664.

[53] A. Zeyer, P. Bahar, K. Irie, R. Schlüter, and H. Ney, "A Comparison of Transformer and LSTM Encoder Decoder Models for ASR," IEEE Xplore, Dec. 01, 2019. https://ieeexplore.ieee.org/document/9004025 (accessed Jul. 31, 2022).

[54] Y.-H. Wu, Y. Liu, X. Zhan, and M. Cheng, "P2T: Pyramid Pooling Transformer for Scene Understanding," IEEE Transactions on Pattern Analysis and Machine Intelligence, vol. 45, no. 11, pp. 12760–12771, Nov. 2023, doi: https://doi.org/10.1109/tpami.2022.3202765.

[55] J. Tang, C. Deng, and G.-B. Huang, "Extreme Learning Machine for Multilayer Perceptron," IEEE Transactions on Neural Networks and Learning Systems, vol. 27, no. 4, pp. 809–821, Apr. 2016, doi: https://doi.org/10.1109/tnnls.2015.2424995.

[56] K. Adem, S. Kiliçarslan, and O. Cömert, "Classification and diagnosis of cervical cancer with stacked autoencoder and softmax classification," Expert Systems with Applications, vol. 115, pp. 557–564, Jan. 2019, doi: https://doi.org/10.1016/j.eswa.2018.08.050.

[57] W. Li, F. Qi, M. Tang, and Z. Yu, "Bidirectional LSTM with self-attention mechanism and multi-channel features for sentiment classification," Neurocomputing, vol. 387, pp. 63–77, Apr. 2020, doi: https://doi.org/10.1016/j.neucom.2020.01.006.

[58] Osolo Ian Raymond, Z. Yang, and J. Long, "An Analysis of the Use of Feed-Forward Sub-Modules for Transformer-Based Image Captioning Tasks," Applied sciences, vol. 11, no. 24, pp. 11635–11635, Dec. 2021, doi: https://doi.org/10.3390/app112411635.

[59] J.-H. Luo and J. Wu, "Neural Network Pruning With Residual-Connections and Limited-Data," arXiv (Cornell University), Jun. 2020, doi: https://doi.org/10.1109/cvpr42600.2020.00153.

[60] B. Cui, Y. Li, M. Chen, and Z. Zhang, "Fine-tune BERT with Sparse Self-Attention Mechanism," ACLWeb, Nov. 01, 2019. https://aclanthology.org/D19-1361/ (accessed Aug. 27, 2023).

[61] N. K. Manaswi, "Understanding and Working with Keras," Deep Learning with Applications Using Python, pp. 31–43, 2018, doi: https://doi.org/10.1007/978-1-4842-3516-4_2.

[62] H. Joodaki and M. B. Panzer, "Skin mechanical properties and modeling: A review," Proceedings of the Institution of Mechanical Engineers, Part H: Journal of Engineering in Medicine, vol. 232, no. 4, pp. 323–343, Mar. 2018, doi: https://doi.org/10.1177/0954411918759801.

[63] H. M and S. M.N, "A Review on Evaluation Metrics for Data Classification Evaluations," International Journal of Data Mining & Knowledge Management Process, vol. 5, no. 2, pp. 01-11, Mar. 2015, doi: https://doi.org/10.5121/ijdkp.2015.5201.

[64] Y. Tai, K. Qian, X. Huang, J. Zhang, M. A. Jan, and Z. Yu, "Intelligent Intraoperative Haptic-AR Navigation for COVID-19 Lung Biopsy Using Deep Hybrid Model," IEEE Transactions on Industrial Informatics, vol. 17, no. 9, pp. 6519–6527, Sep. 2021, doi: https://doi.org/10.1109/TII.2021.3052788.

[65] P.V. Sabique, Ganesh Pasupathy, R. Sivaramakrishnan, and G. Shanmugasundar, "Investigating the influence of dimensionality reduction on force estimation in robotic-assisted surgery using recurrent and convolutional networks," Engineering Applications of

Artificial Intelligence, vol. 126, pp. 107045–107045, Nov. 2023, doi: https://doi.org/10.1016/j.engappai.2023.107045.

[66] Fatemeh Karimirad, S. Chauhan, and Bijan Shirinzadeh, "Vision-based force measurement using neural networks for biological cell microinjection," Journal of Biomechanics, vol. 47, no. 5, pp. 1157–1163, Mar. 2014, doi: https://doi.org/10.1016/j.jbiomech.2013.12.007.

[67] Z. Chua, A. M. Jarc, and A. M. Okamura, "Toward Force Estimation in Robot-Assisted Surgery using Deep Learning with Vision and Robot State," 2021 IEEE International Conference on Robotics and Automation (ICRA), May 2021, doi: https://doi.org/10.1109/icra48506.2021.9560945.

[68] D. L. Packer, S. B. Johnson, M. W. Kolasa, T. J. Bunch, B. D. Henz, and Y. Okumura, "New generation of electro-anatomic mapping: full intracardiac ultrasound image integration," Europace, vol. 10, no. Supplement 3, pp. iii35–iii41, Nov. 2008, doi: https://doi.org/10.1093/europace/eun231.

[69] M. V. Orlov et al., "Direct Visualization of the His Bundle Pacing Lead Placement by 3-Dimensional Electroanatomic Mapping," Circulation: Arrhythmia and Electrophysiology, vol. 12, no. 2, Feb. 2019, doi: https://doi.org/10.1161/circep.118.006801.

[70] R. Das, Nayan Jyoti Baishya, and B. Bhattacharya, "A review on tele-manipulators for remote diagnostic procedures and surgery," CSI Transactions on ICT, vol. 11, no. 1, pp. 31–37, Mar. 2023, doi: https://doi.org/10.1007/s40012-023-00373-2.

[71] S. Y. Ng and C.-L. Lin, "A Multilayered, Lesion-Embedded Ultrasound Breast Phantom with Realistic Visual and Haptic Feedback for Needle Biopsy," Ultrasound in Medicine & Biology, vol. 48, no. 8, pp. 1468–1483, Aug. 2022, doi: https://doi.org/10.1016/j.ultrasmedbio.2022.03.009.

[72] N. Goertzen et al., "Quantum Cascade Laser-Based Infrared Imaging as a Label-Free and Automated Approach to Determine Mutations in Lung Adenocarcinoma," The American Journal of Pathology, vol. 191, no. 7, pp. 1269–1280, Jul. 2021, doi: https://doi.org/10.1016/j.ajpath.2021.04.013.

[73] R. Bhargava, "Digital Histopathology by Infrared Spectroscopic Imaging," Annual Review of Analytical Chemistry, vol. 16, no. 1, pp. 205–230, Jun. 2023, doi: https://doi.org/10.1146/annurev-anchem-101422-090956.

[74] Y. Ran et al., "Fiber‐Optic Theranostics (FOT): Interstitial Fiber‐Optic Needles for Cancer Sensing and Therapy," vol. 9, no. 15, pp. 2200456–2200456, Mar. 2022, doi: https://doi.org/10.1002/advs.202200456.